The Investigation of Flow Rate and Radiation Effects on FaDu Cells

A Comparative Study Using Microfluidic Chips and a Conventional 2D In Vitro Model

Milou Esmee Sengers

Delft University of Technology

TU Delft

The Investigation of Flow Rate and Radiation Effects on FaDu Cells

A Comparative Study Using Microfluidic Chips and a Conventional 2D In Vitro Model

by

Milou Esmee Sengers

to obtain the degree of Master of Science
in Biomedical Engineering, track Medical Physics
at the faculty of Mechanical Engineering
at Delft University of Technology
to be defended on December 1st, 2025.

Supervisors

Prof. Dr. ir. A.G. Denkova	Delft University of Technology
Dr. A. Puspitasari-Kokko	HollandPTC
ir. E. van der Wal	Lyla Systems

Thesis committee

Prof. Dr. ir. A.G. Denkova	Delft University of Technology
Dr. A. Accardo	Delft University of Technology

An electronic version of this thesis is available at `https://repository.tudelft.nl/`.

TU Delft

HollandPTC
Proton Therapy Centre

Acknowledgments

I would like to begin with thanking my daily supervisor Reni. Without her, this project would not have been possible. She helped and guided me a lot throughout the whole project and always made time for me whenever I had a question or needed help and feedback. Next, I would like to thank my TU Delft supervisor Antonia. She was always able to meet with me on short notice and found ways to encourage me throughout the project. I also want to thank my third supervisor, Ernst. He always asked the right questions during our meetings which pushed me to think more critically. He also helped me in looking for solutions whenever a technical problem occurred with my experimental setup.

Moreover, I'm very grateful for Thomas Toet from HollandPTC and Astrid van der Meer from RID for taking the time to assist me with the execution of my radiation experiments.

Furthermore, I would like to thank Angelo Accardo for making the time to be a member in my committee and reading and reviewing my thesis.

I had a very warm welcome and a great time at HollandPTC, which would not have been without my fellow master students Max, Sake and Anna, as well as PhD students Julian, Simone, Anne and Manon, and my friend Anne-Wil. I really enjoyed the coffee and lunch breaks, and especially the Junior Research Borrels, where we discovered new bars and restaurants in Delft. They also listened and tried to come up with solutions whenever I asked, for which I am very thankful.

Lastly, I would like to thank my family and university, rowing and beach volleyball friends for listening, supporting, encouraging and distracting me whenever necessary in the past year. I had many ups and downs, and sharing these with them kept me positive and motivated.

Milou Esmee Sengers
Delft, November 2025

Abstract

Radiotherapy is a frequently used therapy for cancer. However, conventional radiobiological research models used to optimize such therapies are often expensive, ethically challenging or lack human physiological relevance. Therefore, alternative models need to be introduced to overcome these challenges. Microfluidic on-a-chip systems offer much potential, but their application in radiobiology research remains limited. This thesis explores the use of an on-a-chip system and aims to answer the main research question: *"How does flow rate influence the morphology, cell count, nuclear size and proliferation of FaDu cells cultured in an on-a-chip system, and how do these cells respond to photon and proton irradiation compared to conventional static cultures?"*

FaDu cells were cultured on coverslips under static conditions and on-chip under continuous flow rate conditions and irradiated with 2 or 5 Gy X-rays or protons. After fixation and fluorescence staining, cell morphology, nucleus area and proliferation activity were assessed through fluorescence imaging and image analysis.

A flow rate of 500 µL/h reduced cell adhesion. However, the adherent cells showed larger nuclei and higher proliferation activity than coverslip cultures after proton radiation, suggesting that shear stress and the chip environment change cell physiology. Chip-cultured cells also showed clear morphology changes regardless of flow rate. Early morphology radiation effects differed slightly between X-ray and proton exposure under static conditions. Moreover, non-viable cells within the outlet medium were larger on average than the viable cells, indicating that these cells might have been in the G2/M cell-cycle phase, which is more radiosensitive.

Despite challenges such as air bubble formation, limited datasets and image segmentation inaccuracies, the study successfully established a workflow combining microfluidics, irradiation and quantitative imaging. With optimized flow rate conditions, improved staining and imaging procedures, and including co-cultures or 3D tumor models, this on-a-chip setup could become a powerful tool for preclinical radiotherapy research.

Contents

1 Introduction

Cancer is one of the most deadliest diseases worldwide and a heavy burden on society [1]. In 2022, around 20 million new cancer cases were reported, with nearly 10 million deaths. Globally, about 1 in 5 people will develop cancer during their lifetime. It accounts for approximately 1 in 9 deaths among men and 1 in 12 deaths among women. The most common cancer types include lung, breast, colorectal, gastric, liver, cervical, and prostate cancer [2]. Radiotherapy (RT), chemotherapy (CT) and surgery are the most common treatments for cancer patients. RT is frequently used either as a stand-alone treatment or in combination with surgery or CT to ensure complete elimination of tumor cells and reduce the risk of local recurrence.

Radiotherapy

Radiotherapy is one of the most frequently used treatments in oncology, with approximately 50% of cancer patients receiving this treatment. It is estimated that radiotherapy contributes to around 40% of oncological cures, either used alone or combined with other treatments. Its goal is to destroy malignant cells with ionizing radiation locally, while preserving surrounding healthy tissue and organs at risk (OAR). Commonly used ionizing radiations are high energy X-rays. However, photons deliver their highest dose right at the entrance of the body, after which the dose declines. This means that healthy tissue receives unintended radiation, leading to toxic side effect risks.

In contrast, proton therapy has a big advantage. It delivers its dose very locally and almost at the end of their range, called the Bragg peak. This results in sparing the surrounding healthy tissue and OAR and decreasing toxic side effect risks. This is especially beneficial for head and neck cancer patients, due to numerous OAR in that region [3]. Furthermore, proton beams have a higher Linear Energy Transfer (LET) and Relative Biological Effectiveness (RBE), approximately 1.1 compared to 1.0 for X-ray beams, due to differences such as DNA damage effects and repair mechanisms. Despite these benefits, proton therapy is limited by its high costs and technical complexity. Therefore, it is only used for treating complex tumors located close to sensitive OARs, such as those in the skull, head and neck region, spine, breast and eye regions [4, 5].

Radiobiology models

Although cancer treatments continue to improve, significant challenges remain, such as minimizing radiation to healthy tissue, overcoming tumor radioresistance and reducing toxic side effects [6]. A better understanding of radiation responses, such as DNA damage, repair pathways and cell–cell interactions, is still needed to improve the effectiveness of radiotherapy [7]. This research field is known as radiobiology.

Radiobiological studies still rely on conventional 2D cell culture (*in vitro*) models, which have been used since the 1920s [8]. These models are easy to use, cost-effective and suitable for high-throughput screening. They have contributed to understanding basic cellular mechanisms after irradiation, such as DNA damage, cell death and radiosensitizer development, but they lack critical features like correct morphology, dynamic interactions and oxygen perfusion to truly mimic human *in vivo* responses after

irradiation [9].

Animal (*in vivo*) models, such as rodents, overcome several of these limitations and are used to study radiation effects at the whole-organism level [9]. However, they are expensive, time consuming, raise ethical concerns and fail to fully mimic human physiology and radiation dose responses. Therefore, there is a need for new models that reduce the reliance on animal testing while offering a standardized model to advance preclinical radiotherapy research [7, 10].

On-a-chip systems

To overcome these challenges, microfluidic devices have been used to create organ-on-a-chip systems since 2010 [11]. They could serve as a bridge between conventional 2D *in vitro* and *in vivo* models. These systems are able to mimic numerous key human physiological conditions, such as controlled flow rate, mechanical strain and shear stress, which are absent in static cultures, but critical when wanting to create realistic cellular behavior [12]. Several advantages of this model includes reduced experimental costs due to low sample volume, compatibility for high throughput studies and the possibility to analyze real-time cell/tissue responses [6].

A large number of studies have shown that these models can be successfully applied in research areas such as therapy development. However, their application in radiobiology remains limited, despite the need for further research in this field. These systems are able to simulate dynamic conditions such as fluid flow, mechanical stress and nutrient supply, which may influence cellular responses to radiation [6]. Their applications hold potential for studying tumor hypoxia by replicating the tumor microenvironment (TME), investigating radioresistance and radiation effects at tissue and organ levels and even develop patient specific therapies using primary tumor cells or biopsy slices [13].

In this thesis, an on-a-chip system is used for radiobiology experiments, addressing the limited use of such models in this field. The goal is to investigate the effect of flow rate on a head and neck cancer cell line (FaDu; ATCC HTB-43) cultured in the µ-Slide III 3D Perfusion (ibidi; Cat.No: 80376) after irradiation with photons or protons. Results are then compared to FaDu cells cultured on coverslips in a conventional 12-well plate (Greiner BIO-ONE; Cat.No: 665 180), irradiated under the same conditions and without a flow rate. By comparing static and dynamic culture systems, this study aims to provide new insights into how microfluidic platforms can be used and possibly enhance radiobiological research.

Therefore, the main research question of this is thesis is: *"How does flow rate influence the morphology, cell count, nuclear size and proliferation of FaDu cells cultured in an on-a-chip system, and how do these cells respond to photon and proton irradiation compared to conventional static cultures?"*

Thesis outline

In this thesis, Chapter 2 provides the theoretical background needed to understand certain aspect of the project, including radiotherapy, radiobiology, on-a-chip systems and immunocytochemistry florescence. Chapter 3 gives a detailed explanation of the materials and methods used in the flow rate and radiation experiments conducted with the on-a-chip system and conventional coverslips. Afterwards, results will be shown and discussed, including experimental challenges, data analysis limitations and recommendations for future research, in Chapter 4. Lastly, conclusions are drawn in Chapter 5.

2

Background & Theory

2.1. Head and Neck Squamous Cell Carcinoma (HNSCC)

Head and neck cancers (HNC), which mostly originate from the mucosal epithelium of the mouth, larynx, and pharynx, are most commonly diagnosed as head and neck squamous cell carcinoma (HNSCC). Major risk factors include heavy tobacco use and alcohol consumption, as well as infection with human papillomavirus (HPV). Although FDA-approved HPV vaccines are available worldwide and can prevent HPV-related HNSCC, many cases remain HPV-negative [14].

HNSCC is the sixth most common cancer globally, with approximately 900,000 new cases and 450,000 deaths reported in 2018 and is expected to rise each year. The disease occurs two to four times more frequently in men than in women, with a median age at diagnosis of around 66 years. Early detection is limited to only physical examination, as no effective screening methods exist, and a diagnosis relies on biopsy [14].

Treatment strategies vary by disease stage and typically involve surgery followed by radiotherapy or chemotherapy, or a combination of both, which is called chemoradiotherapy (CRT). More recently, immunotherapy has also been introduced. Despite these treatment advances, mortality remains high [14]. The complex tumor microenvironment (TME), primarily hypoxia, which reduces tumor oxygen supply, significantly limits treatment efficacy, especially in radiotherapy [15]. Additionally, tumors often develop radioresistance, leading to recurrence [16]. As a result, the 5-year overall survival rate remains only about 53% [4].

Several recent studies have explored different aspects of radiotherapy in the treatment of HNSCC. These include comparisons of oncologic outcomes of proton therapy and intensity-modulated radiation therapy (IMRT) for HNSCC [17], investigations into how the position within the proton Bragg curve affects DNA damage complexity and cell survival [3] and evaluations of treatment responses using 3D hypoxic cell culture models to improve therapeutic strategies [15].

2.2. Radiotherapy

The main goal of RT is to target and kill cancer cells by directly damaging its DNA through single- and double-strand breaks (SSB and DSB, respectively) using high-energy radiation, while minimizing damage to surrounding healthy tissue as much as possible. This results in cancer cell death through the activation of DNA damage response (DDR), cell cycle arrest and apoptosis. A benefit is that this is a non-invasive treatment, but in comes with drawbacks, such as toxic long-term effects, dose constraints and the development of tumor radioresistance, which can reduce the therapeutic effectiveness [16].

To evaluate the biological impact of different radiation types relative to photons, the concept of Relative Biological Effectiveness (RBE) is used. RBE is defined as the ratio between the dose of photons and other radiation types required to cause the same biological effect. For photons, the RBE value is thus 1.0 [18]. RBE is depended on several factors, including the biological endpoint investigated and can

be experimentally determined by comparing cell survival curves for the same cell line irradiated with a reference photon beam and a particle beam [19].

Linear Energy Transfer (LET) is defined as the average amount of energy deposited by a charged particle per unit length of its path through a medium, commonly expressed in keV/µm. It is a measure of ionization density and is used to characterize the quality of an ionizing radiation beam [20].

There is a wide range of radiation types and delivering techniques in RT that vary in energy, LET, dose rate and RBE. Examples include external beam radiation therapies such as photon intensity-modulated and stereotactic body radiation therapy (IMRT and SBRT, respectively), particle-based therapies such as proton and carbon-ion therapy and internal modalities such as brachytherapy (BT) and radionuclide therapy (RPT) [10, 21].

For HNSCC patients, conventional external beam radiotherapy is typically delivered in daily fractions of 2 Gy for 35 days, resulting in a total dose of 70 Gy. Current research is exploring ways to increase therapeutic effectiveness, such as hyperfractionation, which is delivering twice as much dose in the same treatment period, and accelerated fractionation, which is delivering the same amount of total dose in a shorter period of time. Other studies focus on adaptive radiotherapy, which is adjusting the treatment plan according to anatomical changes in the patient throughout the course of the treatment [22].

2.2.1. X-rays

The most commonly used form of radiotherapy treatment uses high-energy (> 6 MV) X-rays, also called photons, was first clinically used in 1896 [23]. These photons are generated in a linear accelerator (linac), where electrons are emitted from a heated filament (the cathode) and accelerated across the tube containing a high voltage difference towards a metal target with a high atomic number (the anode). The deceleration of the electrons after hitting the anode causes the production of photons. Their energy can be changed by altering the voltage between the anode and cathode. Before the beam exits the machine, it passes through a filter which removes unnecessary low-energy photons [24]. A schematic of this setup is shown in Fig. 2.1.

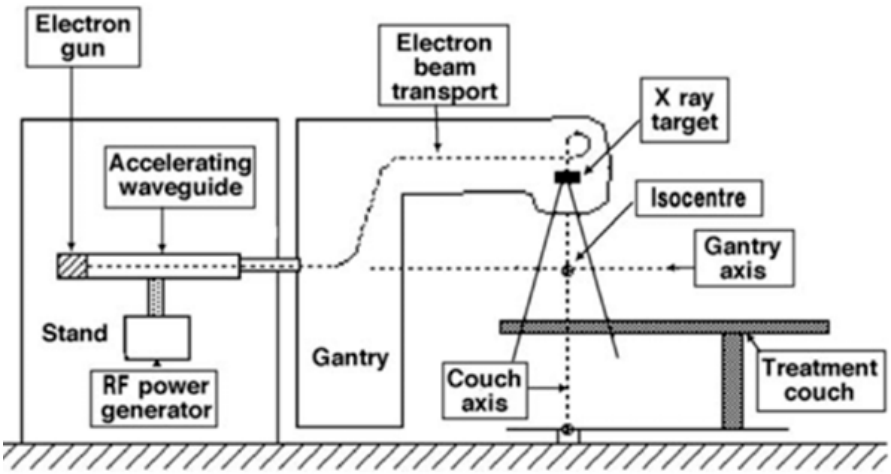

Figure 2.1: Schematic of a medical linac, from [20]

X-ray beams are considered low LET radiations, typically below 1 keV/µm. This means that energy is deposited moderately along their track, which leads to mostly indirect DNA damage, which have faster and easier repair pathways that direct DNA damage [20].

An advantage of photon radiotherapy is that it's relatively cheap, technically easy to produce and non-invasive. However, photons deposit their dose gradually after entering the body, reaching a maximum at a shallow depth beneath the skin, after which the dose decreases with increasing depth, as shown in Fig. 2.2. Due to the physical properties of photons, this is a disadvantage when treating tumors located superficial or deeper within the body, since increasing the tumor dose would also increase the

dose to surrounding healthy tissues that must be spared as much as possible, resulting in a high toxicity. This is especially a problem for tumors located nearby high-risk organs [18]. Acute side effects include localized pain, skin irritation, and fatigue and could occur shortly after treatment. Long-term toxicities include dose-limiting tissue tolerance and an increased risk of developing radiation-induced secondary cancers [16].

2.2.2. Protons

A relative newer radiation technique is proton radiotherapy, which uses positively charged particles (hydrogen ions). Protons have a clear depth–dose distribution, as shown in Fig. 2.2. As protons travel through tissue, they lose energy slowly until they reach a specific depth, where they deposit most of their energy almost at the end of their range, also called the Bragg peak. Beyond this point, the dose rapidly falls to nearly zero, which allows for sparing of tissues located after the tumor [18].

To cover the entire tumor volume, multiple proton beams with different energies are combined, forming a Spread-Out Bragg Peak (SOBP, see Fig. 2.2). This ensures a uniform dose across the tumor while still maintaining a steep dose fall-off beyond the tumor. The position of the Bragg peak depends on the initial proton energy and the tissue density along the beam path, which allows treatment plans to be made precisely to the patient's anatomy [18, 25].

These protons are accelerated to high clinical energies (70-250 MeV) with the use of mostly cyclotrons, which produce high density proton beams of one energy, but also synchrotrons, which produce batches of proton beams of various energies. The shaping and modulation of the beams is achieved through collimators, compensators and scanning magnets that can steer the beam laterally and in depth [25].

The main advantages of using protons over photons is their greater ability to spare healthy surrounding tissue that are located close to the target volume, which makes it very suitable for treating tumors located near radiosensitive tissues, such as in the brain, head and neck, spine and pediatric cancers. This tissue sparing can lead to a reduction in both acute and long-term toxicities, such as secondary cancers, which is especially important in children [5]. Moreover, they are able to deposit a uniform dose to the whole tumor volume [26].

However, there are also several limitations. The high cost and complexity of proton facilities, which means requiring large accelerators and shielding constructions as well as accurate beam delivery systems, limit their availability to specialized centers only. Furthermore, the dose distribution is sensitive to patient setup errors (including patient motion and anatomical changes) and CT artefacts [18].

A difference between proton and photon radiation is their Linear Energy Transfer (LET), which describes the amount of energy deposited per unit length of the tissue covered by the radiation. Proton beams show a low LET at the entrance, similar to photons, but it increases quickly towards the Bragg peak. This increased LET results in denser ionizations and more clustered DNA damage, leading to complex damages that are harder for cells to repair. As a consequence, biological effects vary across the beam path, even if the physical dose is the same [18].

In clinical proton therapy, a constant Relative Biological Effectiveness (RBE) value of 1.1 is used, which means that protons are assumed to be 10% more effective at causing the same biological effect as photons. However, experimental data suggest that RBE is not constant. It increases with LET, decreases with dose per fraction and varies between tissues, cell cycle stage and biological endpoints. Especially near the distal end of the Bragg peak, higher LET and more complex DNA damages could lead to increased cell killing and higher healthy tissue toxicities [18, 19].

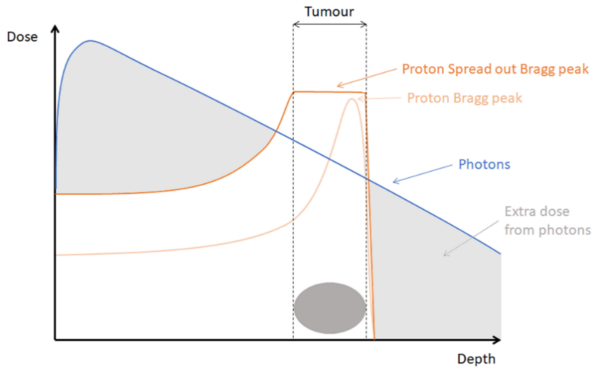

Figure 2.2: The depth-dose distribution of photons compared to protons [18]

2.3. Radiobiology

In the field of radiobiology, research is done on the interaction and effect of ionizing radiation, such as photons or protons, on biological molecules, cells and tissue, both healthy and cancerous. When ionizing radiation interacts with cells, physical effects occurs first, after which chemical and biological processes that can lead to cell damage. The most critical biological target is DNA, which could be damaged either directly or indirectly. Direct damage occurs when radiation deposits energy directly into DNA, which is more common with high-LET radiation. Indirect damage, which mainly occurs with low-LET radiation, is caused by the interaction of radiation with water other molecules, leading to the production of reactive oxygen species (ROS) and free radicals that subsequently damages DNA [20].

Depending on the radiation type and dose, several biological outcomes are possible, including delay in division, apoptosis, reproductive failure, genomic instability, mutation, transformation, bystander effects, adaptive responses and no effect [20]. Current research in radiobiology aims to obtain a deeper understanding of these mechanisms, including DNA damage and their repair pathways, radiation-induced toxicity, cell survival and death, and tumor radioresistance [21, 27, 28].

Understanding these processes is important for improving the effectiveness of radiotherapy, as well as for interpreting how specific conditions, such as flow rate, shear stress or oxygen supply, may influence biological radiation responses and treatment outcomes.

2.3.1. DNA damage and repair

Ionizing radiation can affect many cellular components, but DNA damage within the cancerous cell is the most important biological target, due to the fact that radiation-induced DNA damage can change normal cellular function and when unrepaired, could lead to cell mutation or death [20].

Radiation induces different types of DNA damages, including single-strand breaks (SSBs), double-strand breaks (DSBs) and base and sugar modifications, as shown in Fig. 2.3. SSBs can be caused by indirect ionization of DNA and DSBs by direct ionization of DNA and can range from single to clustered damage sites and complex DSBs [29]. Among these, DSBs are considered the most biologically significant, since they are difficult to repair correctly and can result in cell death.

DSBs increase with increasing radiation dose. Another factor influencing the amount of DNA damage is LET. High-LET radiation, such as protons, can results in denser ionization events which causes more clustered DNA damage compared to low-LET radiation, such as photons, which induces damage primarily through indirect damage mechanisms. DNA damages caused by high-LET are more difficult to repair [18]. Moreover, ionizing radiation given in fractions increases the number of clustered DNA damages [29].

Cell repair DSBs mainly through two pathways, namely non-homologous end joining (NHEJ), which is the major and faster but more prone to errors mechanism working throughout the whole cell cycle, especially the G1 phase, and homologous recombination (HR), which is slow but provides a greater chance to correct reparation and is restricted the G2 and S phases [16]. Most DSBs induced by low-LET

radiation are repaired within 30 to 60 minutes, whereas a small fraction with more complex damages is repaired after several hours, or even longer than 24 hours. It is said that when LET increases, the number of slower repairing cells increases and thus the overall damage complexity as well. When DNA replication fails, replication-induced DSBs may occur, which can be detected as RAD51 foci, typically after 2 to 3 hours after irradiation. The efficiency and accuracy of these repair mechanisms determine whether a cell successfully recovers or undergoes death [29].

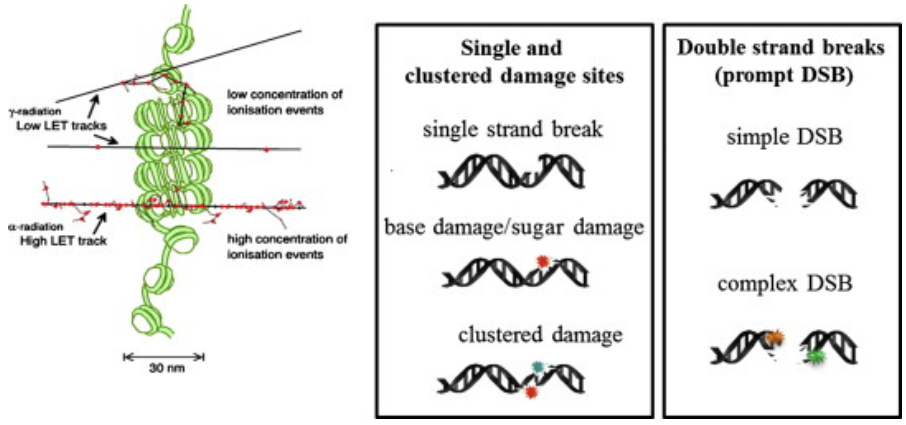

Figure 2.3: Types of radiation-induced DNA damage caused by a single radiation track. The red and green stars represent base or sugar damage [29]

2.3.2. Cell survival and death

The biological outcome of radiation exposure is thus dependent on the amount of DNA damage and how well a cell can repair this. Depending on the severity and type of damage, cells can either survive and keep their functionality, undergo programmed or accidental death, or obtain permanent mutations. The main types of radiation-induced cell death include mitotic catastrophe, apoptosis and necrosis. Mitotic catastrophe occurs when cells attempt to divide with unrepaired DNA damage, leading to triggering mitotic arrest which could lead to cell death. Apoptosis is programmed cell death, which occurs typically in radiosensitive tissues or early after high-dose radiation exposure and is highly regulated. In contrast, necrosis is a passive and unregulated type of cell death and is associated with very high radiation doses. The type of cell death is mainly determined by the cell and radiation type [18].

The relationship between dose and the fraction of surviving cells (also known as the cell survival curve) is typically described by the linear-quadratic (LQ) model:

$$S(D) = e^{-(\alpha D + \beta D^2)}, \tag{2.1}$$

where *S(D)* represents the surviving fraction of cells after a dose D (Gy) and α and β are the linear and quadratic components of radiation-induced cell killing, respectively. The shape of the cell survival curve is influenced by the radiation type and is determined by *in vitro* or *in vivo* techniques. This model can be used to quantify radiosensitivity and to compare biological effectiveness among different radiation types [20].

As mentioned before, there are several factors that change the radiosensitivity of cells, including the amount of oxygen within a cell, radiation quality (such as LET), cell cycle phase, temperature and DNA repair capacity. Cells in the G2/M phase or under normal oxygen conditions are generally more sensitive to radiation, while hypoxic cells and successful repair mechanisms lead to lower radiosensitivity [20]. In the next section, several of these factors will be discussed.

2.3.3. Radioresistance

There are several mechanisms that reduces the chance of a cancer cell dying from ionized radiation, also called radioresistance. Consequences include the recurrence of tumors or the spreading of cancer cells (metastasis) and decrease the chance of long-term survival for cancer patients undergoing RT. It

is therefore important to overcome radioresistance to enhance treatment outcomes. These mechanisms include hypoxia, enhanced DNA repair, cell cycle phase and the activity of the tumor microenvironment [16, 20]. Fig. 2.4 shows the main mechanisms for radioresistance in tumors.

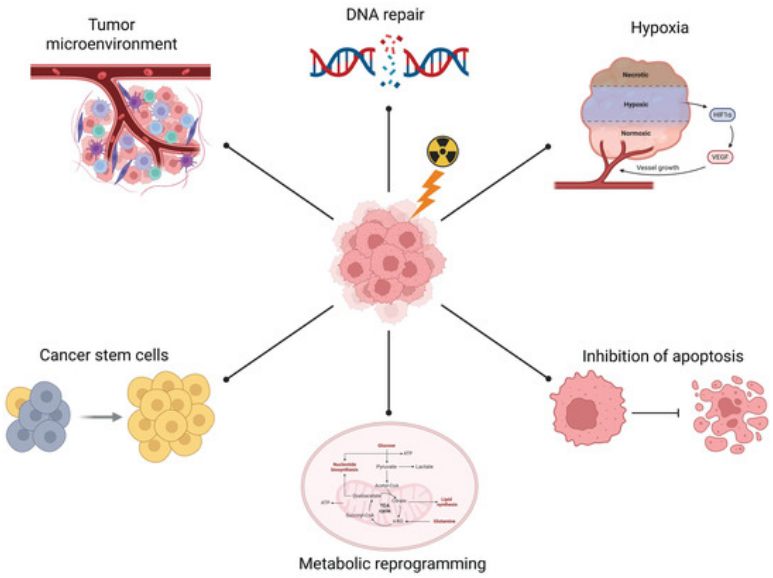

Figure 2.4: Several mechanisms for radioresistance in tumors [16]

Cell cycle phase

The cell proliferation cycle is a cycle with four stages, see Fig. 2.5. It consists of mitosis (M phase), where cell division takes place, and the period of DNA synthesis (S phase). These are separated by two gap phases, namely G1 (cell growth) and G2 (preparation for mitosis). The time between complete division (mitoses) is called the cell cycle time. For most mammalian cells grown *in vitro*, the S phase typically lasts 6 to 8 hours, M phase less than 1 hour, G2 around 2 to 4 hours and G1 around 18 hours. The total cell cycle time is therefore 10 to 20 hours. Cells exiting the active cell cycle enter the G0 phase, which is a phase in which cells do not proliferative [20]. For FaDu cells, the cell proliferation cycle time has been reported to be approximately 18 hours during exponential phase (in which cells are actively and consistently proliferating) in static *in vitro* conditions [30].

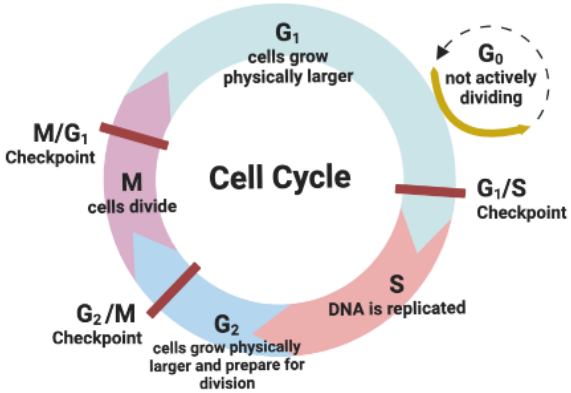

Figure 2.5: Overview of the mammalian cell cycle with its main phases [31]

Radiosensitivity varies throughout the cell cycle. Cells are generally more sensitive to radiation during the M and G2 phase and most radioresistance in the late S phase. This variation is because of the

efficiency of DNA repair mechanisms available at different points in the cycle. After replication, both NHEJ and HR are active, increasing the repair activity and cell survival. In contrast, cells in the M phase are highly radiosensitive due to the reduction in DNA damage repair mechanisms. Cells in the G0 phase are generally less radiosensitive than proliferating cells due to their low metabolic activity and efficient DNA repair mechanisms capacity [20, 32].

For low-LET radiation such as X-rays, this cell cycle-dependent radiosensitivity is has been observed, with higher survival rates of cells irradiated in the late S phase compared to the G1 or M phase. This could be explained by the availability of repair mechanisms after replication. For high-LET radiation such as protons, it is thought that this cell-cycle dependency disappears. However, little research has been done on cell-cycle radiosensitivity after high-LET radiation exposure [32].

Understanding this cell cycle-dependent radiosensitivity is clinically important, since tumors and normal tissues often differ in their cell cycle distributions and proliferation rates. This could influence radiation responses and therefore treatment outcomes [32].

Hypoxia in the tumor microenvironment

The tumor microenvironment (TME), the area in which the tumor is located, is complex and includes numerous cells, such as immune cells, cytokines and cellular metabolites. One of the main hallmarks of the TME is hypoxia, which is the result of low oxygen supply to proliferating tumors. Many solid tumors, including HNSCC, contain hypoxic regions due to abnormal vasculature and limited oxygen supply and consumption. Tumors under hypoxic conditions can recover better from radiation-induced damages and are thus more radioresistant. This poses a problem in RT as it reduces therapeutic effectiveness [15]. In on-a-chip systems, the presence or absence of flow rate can influence oxygen and nutrient supply, potentially mimicking *in vivo* hypoxic conditions and influence observed radiation responses.

2.3.4. Radiobiology models

Radiobiology models are important tools for studying how ionizing radiation interacts with biological systems. They are used to investigate mechanisms such as DNA damage and repair, cell death and tissue responses, as well as to optimize radiotherapy treatments before clinical application. This is important since photon and proton irradiation for example vary in radiobiology, e.g. in RBE and radioresistance, when DNA damage responses and cell death is activated, cell cycle distribution and the creation of ROS [18]. These radiobiology models vary in complexity, from simple 2D cell cultures (monolayers) to 3D cultures, such as organoids, and animal models, each having its own advantages and limitations depending on the research topic [9].

2D monolayer cell cultures are among the most commonly used *in vitro* systems in (radio)biology. They have been used since the 1920s and offer simplicity, reproducibility, high-throughput screening and compatibility with traditional assays [8]. Because they allow for controlled irradiation and straightforward data interpretation, they have been fundamental for understanding basic cell behavior post irradiation and could be used for initial screening of potential radiosensitizing agents [9].

However, 2D models fail to mimic cell morphology and physiological complexity of *in vivo* tissues and lack mechanisms that are known to influence radiosensitivity. As a result, their translational relevance to tumor and normal tissue responses in patients after radiation is limited [9, 10].

Animal models, on the other hand, offer the ability to study systemic effects of radiation, including immune responses and late tissue toxicities. They provide a closer model to human physiology and have been critical for studying dose-limiting toxicities and the biological effectiveness of various radiation types. Nonetheless, these models come with significant drawbacks, as they are costly, time-consuming and raise ethical concerns. Therefore, the 3Rs have been introduced in 1959 to replace, reduce and refine animal models [9, 28].

To overcome the limitations of traditional 2D cultures, 3D cell culture systems have been developed. These include scaffold-based and scaffold-free models, such as spheroids and organoids, which better replicate the tumor microenvironment, such as cell–cell interactions. They can be combined with microfluidics to obtain gradients in oxygen and nutrients within 3D structures, which allows for more realistic modeling of hypoxic tumors, which are known to be more radioresistant, as mentioned in the

previous section [27]. These models are increasingly used to develop personalized models to test RT responses on patient-derived tissues [9].

Despite these advantages, 3D models still lack the dynamic physiological conditions and control found *in vivo*, such as fluid flow, shear stress and oxygen perfusion, which all influence the radiosensitivity and repair processes of cells [9, 10].

Recent advances in microengineering have led to the development of microphysiological, or organ-on-a-chip (OoC), systems. These platforms enable co-culture of multiple cell types under controlled flow rate, oxygen, and nutrient conditions, reproducing tissue interfaces and microenvironmental gradients. They can incorporate mechanical stimuli and real-time monitoring, making them valuable for studying radiation effects and patient-specific responses, while reducing reliance on animal models. OoC systems therefore represent a promising bridge between conventional in vitro and in vivo models [27, 9]. The application of these systems in radiotherapy research will be discussed in the next section.

2.4. On-a-chip systems in RT

Organ-on-a-chip (OoC) systems, originating from microelectronics, could bridge the gap between static *in vitro* and animal models (*in vivo*) [33]. These microfluidic devices, fabricated using techniques similar to those in the computer chip industry [34], operate with µL to mL volumes of fluid precisely and actively controlled by syringe or peristaltic pumps [35]. By allowing the co-culture of multiple cell types and integrating physiological forces like shear stress, OoCs can more accurately replicate organ functions and disease states than conventional 2D models [36]. Since the first lung-on-a-chip was introduced by Huh et al. in 2010 [11], these systems have been developed further and applied in drug testing, toxicity assessment and personalized medicine [37, 38]. Current applications include liver-on-a-chip models for hepatotoxicity studies [39, 40], intestine-on-a-chip platforms for drug absorption research [41, 42] and tumor-on-a-chip systems to study cancer metastasis [43].

In the field of radiobiology, there is still much to explore, such as improving tumor targeting, reducing long-term toxic side effects and gaining a deeper understanding of the interaction between radiation and biological environments [7]. On-a-chip systems could play an important role in investigating relevant biological endpoints in radiobiology, such as studying tumor and normal tissue responses to RT and the effectiveness of novel radiation therapies [10, 39]. An overview of these systems integrated in RT studies can be seen in Fig. 2.6.

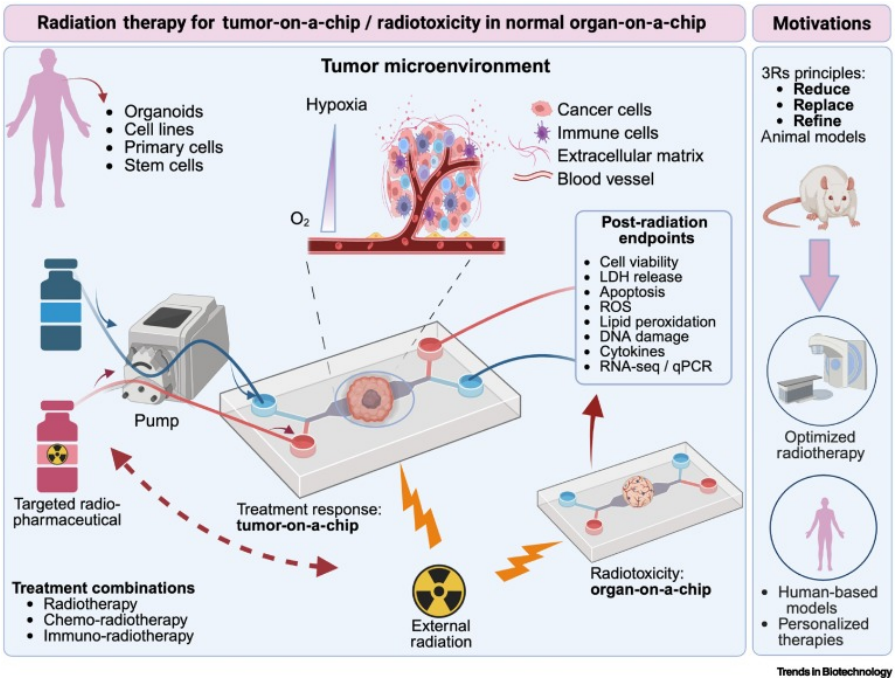

Figure 2.6: On-a-chip system in RT [10]

Importance of fluid flow

As mentioned before, these on-a-chip systems use very small volumes of fluids. With the use of pumps, they can create laminar flow inside the channels and wells. Laminar flow is defined as the movement of liquids without turbulences and is present in many healthy vessels. This enables the generation of the mechanical force shear stress (force per area) to the cells. *In vivo*, it is induced by the parallel friction of liquids against the surface of cells [10]. This mechanical force is a physiological relevant condition due to its impact on cell behavior and adhesion. Furthermore, it changes the cell's gene expression, morphology and physiology, as well as cell layer organization [44].

Shear stress influences cells largely through the cytoskeleton and focal adhesions, which form the link between the cell and its extracellular environment. Focal adhesions are multi-protein complexes that act as mechanical force transmitters. When shear stress is applied, these focal adhesion contacts can reshape, by either getting stronger to increase attachment or by disassembling when the mechanical force is too strong to remain attached. This reshaping affects the cytoskeletal organization, which causes changes in cell spreading, tension and shape [45]. In these on-a-chip systems, shear-induced cytoskeletal reorganizations can therefore alter how well cells remain attached.

Applications in RT

Recent studies have demonstrated the potential of on-a-chip systems to investigate radiation-induced biological responses under physiologically relevant conditions. For example, Staicu et al. developed a glass microfluidic system to study the response of various doses of X-ray radiation on human melanoma cells by measuring their production of reactive oxygen species (ROS), which is a marker for oxidative damage to cells [46].

Carr et al. used 35 HNSCC biopsies from patients to study their response to X-ray radiation of 2 and 40 Gy. They measured the release of lactate dehydrogenase (LDH) in the perfused medium, which was applied at a flow rate of 2 µL/min, for several days, which is a marker for cell death [47]. A follow-up study, where they used biopsies from 5 patients exposed to X-ray radiation ranging from 0 to 20 Gy, showed that there is a variability in cell death and DNA damage outcome between patients [48]. These outcomes highlight the value of patient-derived on-a-chip systems for studying individual radiosensitivity and therapeutic response variability.

Furthermore, it is also feasible to combine RT with chemotherapy (CT) with these on-a-chip systems, which is also commonly done in the clinic and therefore an advantage of these systems [10]. For example, Patra et al. and Bavoux et al. developed PDMS microfluidic systems to culture 3D soft tissue sarcoma (STS) spheroids, which allows for simultaneous exposure to radiation and chemo [49, 50]. Their studies demonstrated that it's possible to quantify radiation-induced apoptosis, investigate cell death pathways and identify potential radiosensitizers that could enhance therapeutic effectiveness.

Advantages and limitations

These on-a-chip systems offer several advantages over conventional *in vitro* and *in vivo* models. Their small size and low fluid consumption make them cost-effective and efficient, while integrated pumps enable controlled perfusion of fresh medium containing nutrients and oxygen, mimicking physiological conditions. Furthermore, the commonly used fabrication material PDMS, is ionizing radiation resistant and stays stable after being irradiated with therapeutic doses. High-penetration radiation, such as X-rays and protons, can pass through PDMS to reach the adhered cells and tissue. For low-penetration radiation, such as alpha particles and low-energy beta emitters, can be perfused directly into the chip's channels to mimic localized RT [10]. Additionally, the on-a-chip design allows real-time monitoring of cell behavior and treatment responses, resulting in faster experimentation [51, 52]. Moreover, by co-culturing multiple cell types, they can be extended into multi-organ or even body-on-a-chip platforms, promoting personalized and precision medicine [33].

Despite these advantages, challenges remain. Commonly used materials such as PDMS can absorb small hydrophobic molecules which can alter experimental results [53]. Furthermore, air bubble formation and the lack of standardized protocols can affect reproducibility and comparability between studies [51, 34].

2.5. Immunocytochemistry fluorescence

It is important to be able to integrate analytical assays in the on-a-chip system to study radiation effects on cells. In order to evaluate and quantify parameters such as DNA damage, cell death, morphology and proliferation, cells can be analyzed using immunofluorescence staining, which can be performed directly on-chip. This can be done with either a primary antibody combined with a fluorescent labeled secondary antibody, or with the use of direct fluorescent stains that bind to specific cellular components, such as the nucleus. Both approaches enable the visualization of the marker under a fluorescence microscope [10]. Below are the markers explained used in this thesis.

γ-H2AX

The first marker is γ-H2AX. It is a marker for DNA DSBs, formed when the histone variant H2AX becomes phosphorylated at the sites of DNA damage [10, 54]. The primary γ-H2AX antibody used in this thesis was raised in rabbits and targets human proteins and is visualized using a fluorophore-conjugated secondary antibody such as Alexa Fluor 647, which was raised in goats and targets rabbit antibodies. This secondary antibody emits red fluorescence (647 nm), causing DNA-damage foci to appear as clear red spots under an immunofluorescence microscope.

The appearance and intensity of γ-H2AX foci are cell-cycle dependent. Cells in S and G2 phases generally show more foci due to active DNA replication and repair, while G1-phase cells display fewer foci [55]. This variability highlights the importance of considering the cell-cycle stage when quantifying γ-H2AX as a measure of radiation-induced DNA damage. Furthermore, γ-H2AX staining is commonly used to study DNA repair kinetics, as the disappearance of foci over time reflects the efficiency of DSB repair processes after irradiation [10, 54].

Ki-67

The second marker is Ki-67. It is a nuclear protein commonly used as a marker for cell proliferation. It expresses in the active phases of the cell cycle (G1, S, G2 and M phases), but absent in resting cells (G0 phase), making it a good marker for detecting proliferating cells [56]. The primary Ki-67 antibody used in this thesis is raised in mice and targets human Ki-67. To visualize it, the fluorophore-conjugated secondary antibody used in this thesis was Alexa Fluor 488, which is raised in goats and targeting mouse antibodies. This fluorophore emits green light (488 nm), which show cell nuclei as green under an immunofluorescence microscope when actively proliferating.

Ki-67 staining could provide valuable information on cell proliferation after irradiation or experimental conditions, such as flow rate, in on-a-chip system.

Phalloidin-TRITC

The third marker is Phalloidin-TRITC. Phalloidin conjugated with Tetramethylrhodamine (TRITC) is used to stain filamentous actin (F-actin), a component of the cytoskeleton responsible for maintaining cell shape, enabling mobility and supporting intracellular transport. Phalloidin binds to F-actin filaments, which allows clear visualization of the actin cytoskeleton and thus the cell's morphology. Since it is a direct stain, it does not require a primary or secondary antibody. When labeled with TRITC, the conjugate emits a red fluorescence signal after excitation, which can be visualized using a fluorescence microscope [57].

Hoechst 33528

The last marker used is Hoechst 33528, which is a commonly used marker to visualize cell nuclei of live and fixed cells using fluorescence microscopy. It is used to assess nuclear morphology, cell count and cell cycle distributions. It emits a blue color after excitation with ultraviolet (UV) light [58].

Each fluorescent marker used in this thesis, so Alexa Fluor 647 (for γ-H2AX), Alexa Fluor 488 (for Ki-67), Phalloidin-TRITC and Hoechst 33258, has specific excitation and emission spectra that determine the color observed under fluorescence microscope. Fig. 2.7 shows typical excitation and emission spectral profiles. When excited by light of a specific wavelength, fluorophores emit light at another wavelength which produces the visible fluorescence signal. It is therefore important to properly select fluorophores with minimal spectral overlap in order to simultaneously detect multiple targets without signal interference [59].

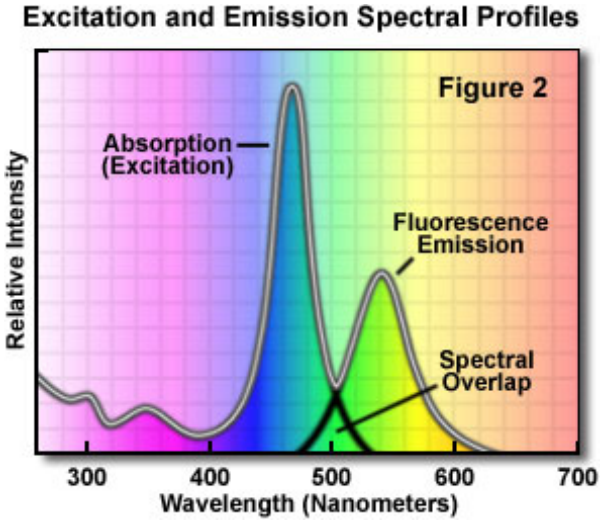

Figure 2.7: Typical fluorochrome excitation–emission spectrum showing excitation, fluorescence emission and spectral overlap, which are important to consider when selecting stains such as Alexa Fluor 647, Alexa Fluor 488, TRITC and Hoechst for simultaneous fluorescence imaging [59]

3

Materials & Methods

This chapter presents an introduction to the overall experiment and provides a detailed explanation of the materials and methods used for cell seeding, the flow rate and radiation experiments and the procedures for data acquisition and analysis.

3.1. Experimental setup

All experiments were conducted using the ibidi µ-Slide III 3D Perfusion (Cat.No: 80376), with results compared to those obtained using Greiner BIO-ONE's 12-well cell culture plate (Cat.No: 665 180). This particular slide was chosen because it contains multiple wells connected by separate channels, allowing for parallel usage. The top two rows were maintained under static conditions (serving as a control), while the bottom row was exposed to flow rate. A schematic drawing of the chip used in the experiments can be seen in Fig. 3.1.

In this setup, reservoir C serves as the inlet and reservoir F serves as the outlet of the medium. Each reservoir (labeled 1) has a capacity of 60 µL. The middle section of the chip contains the wells (labeled 3), each with a diameter of 5 millimeter (mm), a height of 1.2 mm, a volume of 30 µL and a growth area of 25 mm^2. These wells are connected to their reservoirs by channels (labeled 2) that are 1 mm wide.

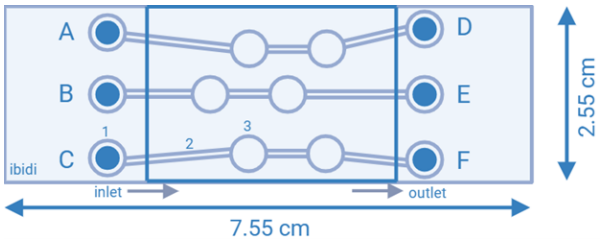

Figure 3.1: Schematic drawing of the ibidi µ-Slide III 3D Perfusion, where label 1 is the reservoir, label 2 is the channel and label 3 is the well. The outer dimensions are 7.55 by 2.55 cm. Created in https://BioRender.com

An important step before conducting the experiments is cell passaging. FaDu (ATCC HTB-43) cells are cultured in 25 or 75 cm^2 cell culture flasks and need to be passaged into a new flask every few days, depending on the dilution of the size of the culture flask, cell mixture and cell culture medium. The cell culture medium used in the testing phase of the flow rate experiments and every cell passage before and in between these experiments is PAN Biotech Ham's F10 medium (Cat.No: P04-13512) mixed with 10% Fetal Calf Serum (FCS) and 1% penicillin/streptomycin (Penstrep). The cell culture medium used afterwards, so in every radiation experiment and cell passage in between these experiments is Capricorn Scientific DMEM High Glucose (4.5 g/L, with Stable Glutamine and Sodium Pyruvate, Cat.No:DMEM-

HPSTA) mixed with 10% FCS and 1% Penstrep. A frequently used dilution between experiments is 1:10 for a 75 cm^2 flask, which, after observation under a microscope (KERN OCM 161), typically results in the flask reaching approximately 75% surface coverage by cells within 6 to 7 days. It is important that the cells maintain consistent growth behavior and doubling times between passages. Therefore, cells should be passaged while they are still actively proliferating to ensure reproducible growth conditions during all experiments. Therefore, a total surface coverage in the flask is not desired and should be avoided. A step-by-step protocol for cell passage can be found in Appendix A.1.1.

Fig. 3.2 and Fig. 3.3 provide a clear overview of the experimental workflows. For the 12-well plate, the workflow is as follows: On day one, FaDu cells were seeded into the wells (a detailed description of this process is given in Section 3.2). The plate was then placed into an incubator (at 37 °C and 5% CO_2) for 48 hours. After this incubation period, so on day 3, the plate was irradiated with either photons or protons with 2 or 5 Gray (Gy), as described in detail in Section 3.4. After radiation, the plate was returned to the incubator for 2 additional hours. Afterwards, the coverslips were fixated inside the wells and stored in the refrigerator (at 4 °C). Staining and imaging the coverslips was carried out at any time after fixation. These procedures are explained in detail in Section 3.5.

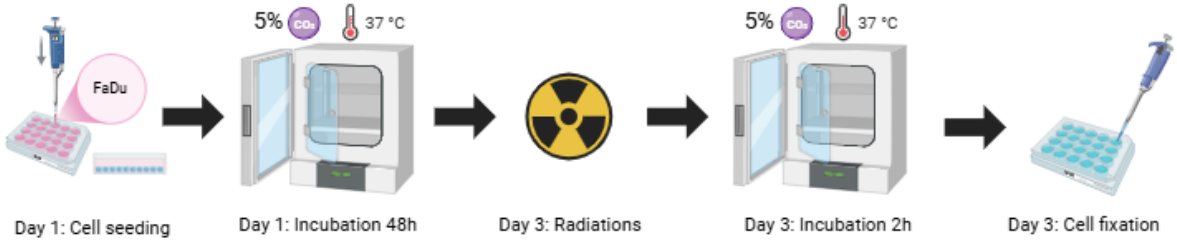

Figure 3.2: Workflow of the 12-well plate, which is used as a control. On day one, cells are seeded into the wells and the plate is placed inside a incubator at 37 °C with 5%CO_2 for 48 hours. On day 3, the plate is irradiated with either photons or protons. Afterwards, the plate is placed inside the incubator again for 2 hours, after which the cells are fixated. Created in https://BioRender.com

For the ibidi chip, the process slightly differs due to the addition of the flow rate setup. On day one, FaDu cells were seeded into the wells of the chip, which was then placed inside the incubator for 24 hours. On day two, flow rate was applied for 20 hours, continuing into the following day. These steps are described in more detail in Section 3.3. On day three, the chip was irradiated with either photons or protons with 2 or 5 Gy, followed by another 2 hours of flow rate. After this, the chip was fixated and stored in the refrigerator. As with the 12-well plate, staining and imaging was carried out at any time after fixation.

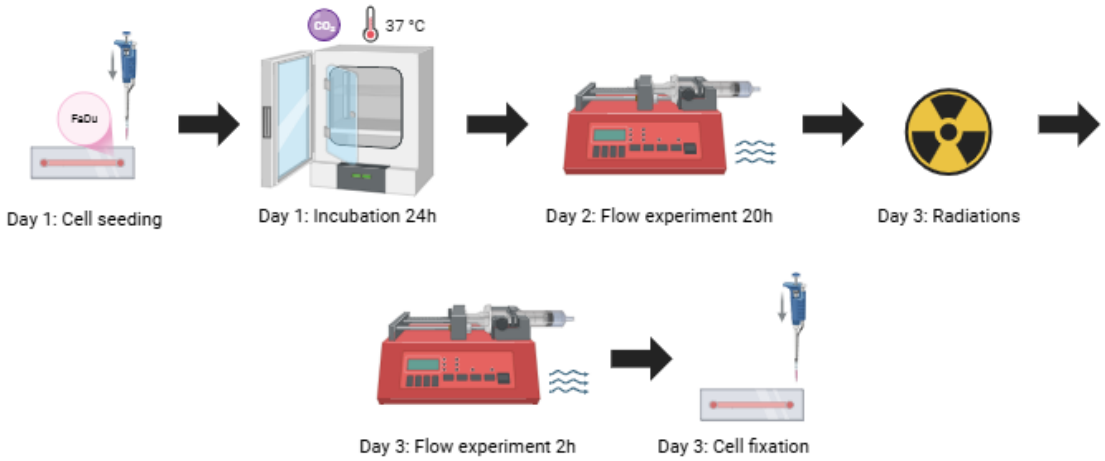

Figure 3.3: Workflow of the ibidi chip. On day one, cells are seeded onto the chip and is placed inside the incubator for 24 hours. On day 2, flow rate is applied for 20 hours. On day three, the chip is irradiated with either photons or protons and flow rate is applied afterwards again for an additional 2 hours. Afterwards, the cells are fixated. Created in https://BioRender.com

Table 3.1 gives an overview of all conducted experiments from which data will be acquired, which is 10 in total.

Table 3.1: Overview of experimental conditions, which could include either flow rate or no flow rate, exposure to either photon or proton irradiations at 2 or 5 Gy and if it's used as a control group or not

Culture System	Radiation Type	Dose (Gy)	Condition
12-well plate (no flow rate)	None	0	Control (no radiation)
	Photons	2 & 5	Irradiated
	Protons	2 & 5	Irradiated
Chip (with flow rate)	None	0	Control (no radiation)
	Photons	2 & 5	Irradiated
	Protons	2 & 5	Irradiated

3.2. Cell seeding

To seed FaDu cells onto the ibidi chip and the 12-well plate, a flask with 75% cell coverage mixed with medium is required. The same steps for cell passage were followed, continuing until the 4 milliliter (mL) cell mixture is collected in a tube. From there, 20 µL of the cell mixture and 20 µL of a viability dye (Bio Rad, Trypan Blue Dye, Cat.No: 1450013) was mixed and pipetted into a Countess slide, see Fig 3.4a. The slide was then inserted into the Countess 3 Automated Cell Counter (ThermoFisher, Cat.No: AMQAX2000). This showed the cell concentration (cells/mL) and the percentage of live and dead cells.

According to ibidi's guidelines, the recommended cell concentration for seeding on the chip is 0.7 - 1.7 $\times 10^5$ cells/mL. The cell mixture obtained after passaging was diluted from 1.0 $\times 10^6$ cells/mL to a concentration of approximately 1.0 $\times 10^5$ cells/mL with medium, using the Countess 3 built-in dilution calculator. Then, 30 µL of this cell mixture was added to each well of the ibidi chip.

For the 12-well plate, an 18 mm glass coverslip was first placed into the middle 6 wells (this is smaller than the diameter of the well, which is approximately 22 mm). Then, 150 µL cell mixture was added on top of the coverslip, followed by 1 mL of cell culture medium. This cell mixture volume was chosen based on scaling the recommended cell mixture for the surface area of the wells of the ibidi chip (25 mm^2) to the larger surface area of the coverslip (2.5 cm^2).

To prevent evaporation during incubation, the other 6 unused wells in the 12-well plate were filled with 1 mL of Phosphate Buffered Saline (PBS)(Sigma-Aldrich, Cat.No: D8537). After closing the plate with

the lid, it was placed inside the incubator for 48 hours.

For the chip it was important to fill each reservoir with 50 µL medium to prevent the wells from drying out. Then, the chip was placed inside a petri dish containing a tissue moistened with 3 mL of PBS, also to prevent the wells from drying out, as shown in Fig 3.4c. After placing the lid on top, it was placed inside the incubator for 24 hours. After incubation, the cells are expected to be attached to the surface of the coverslip in the 12-well plate and to the bottom of the wells in the chip.

A detailed step-by-step protocol for seeding the cells onto the chip and 12-well plate can be found in Appendix A.1.2.

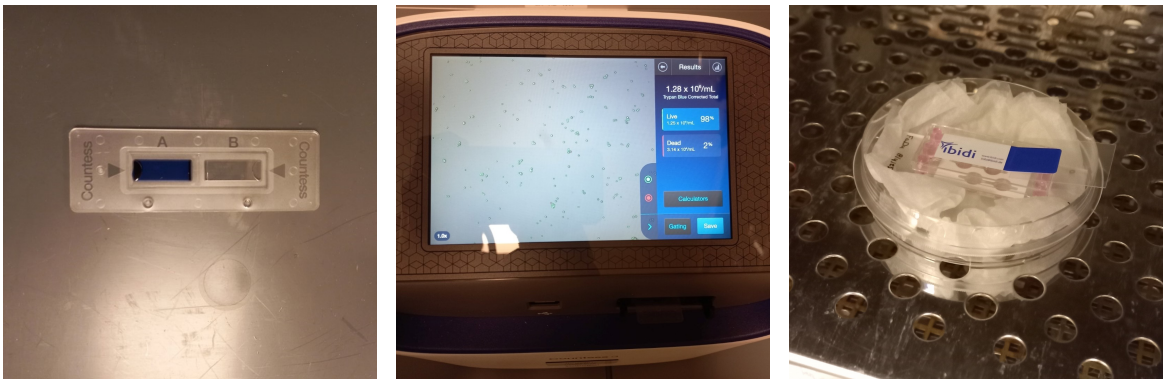

(a) **(b)** **(c)**

Figure 3.4: Cell seeding steps, where (a) shows the Countess slide where only A is filled with the viability dye mixed with the cell solution, (b) shows the Countess screen which shows the amount of cells present in the cell solution (cells/mL) and the percentage of live and dead cells and (c) shows the ibidi chip placed inside the incubator after cell seeding

3.3. Experimental setup for on-a-chip system with flow rate

For this experiment, a syringe pump (KF Technology, model: NE-1000) was used together with a 10 mL syringe holding the cell culture medium. A 0.5 x 16 mm needle (BD Microlance 3, Cat.No: 300600) was connected to the syringe, followed by a segment of silicone tubing (ibidi, Cat.No: 10841) with a length of approximately 54.5 cm, which was secured with a small piece of Parafilm. This tubing was connected to an Elbow Luer connector (ibidi, Cat.No: 10802). A second piece of tubing of approximately 44.0 cm long, also connected to an Elbow Luer connector, served as the outlet and was inserted into a 50 mL centrifuge tube. The tubing was taped in place to make sure it is stable. Since only one pump is available, a flow rate was applied only to the lower wells of the ibidi chip.

After the chip had been inside the incubator for 24 hours, the wells were closed using a No. 1.5 ibidi Polymer Coverslip (0.18 mm thick), taped to the glass lid (see Fig. 3.4(c)). The protective foil on both the chip and the coverslip was removed with tweezers, after which the sticky side of the coverslip was placed on top of the wells and pressed down with a finger to ensure a complete seal.

Before connecting everything to the chip, both inlet and outlet tubings, as well as their connectors, were completely filled with medium to minimize the risk of bubble formation in the wells. The connectors were then attached simultaneously to the left and right reservoirs of the chip. The chip was then placed in a petri dish containing a PBS-moistened tissue to prevent evaporation. Afterwards, the setup was transferred to the incubator along with the 50 mL outlet tube. The syringe itself was mounted in the syringe pump, which was placed outside the incubator. Fig. 3.5(a) shows the setup where the inner door of the incubator is closed. It was necessary to place two pipette tips on both sides of the tubing in between the door and the incubator, to prevent the door from squeezing the tubing. This was also necessary for the outer door, as shown in in Fig. 3.5(b), which also shows a close-up of the syringe pump.

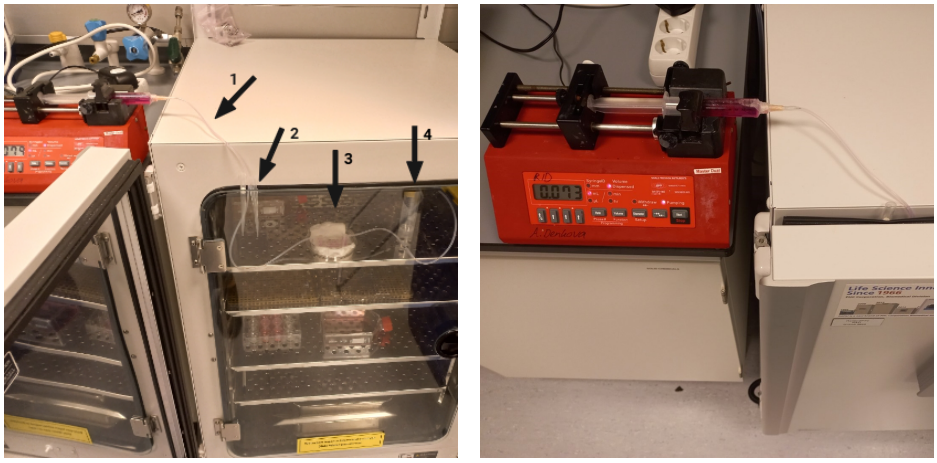

(a) **(b)**

Figure 3.5: Complete experimental setup shown in (a). Arrow number 1 shows the tubing, number 2 the pipette tips used to prevent the tubing from being squeezed by the glass door, number 3 the ibidi chip placed inside a petri dish and number 4 the 50 mL outlet tube. (b) shows a close-up of the syringe mounted into the syringe pump and the outer door of the incubator closed

Several parameters of the syringe pump were set before starting the experiment. First, the flow rate was set to 500 µL/h. At this rate, each well has a complete volume renewal every 3.6 minutes. Second, in this experiment, continuous flow rate was chosen, which is confirmed when the display shows 'OFF' after pressing the Volume key. Third, the syringe's inner diameter of 15 mm was entered. Finally, the pumping direction 'infusion' was selected, which was active when the 'Withdraw' LED was not illuminated. Once the syringe was mounted onto the pump and all settings were applied, the pump was started by pressing the 'Start/Stop' key.

To allow enough time for observing potential differences between cells exposed to a flow rate versus no flow rate, a pumping duration of 20 hours was selected. At a flow rate of 500 µL/h, this resulted in a total volume of 10 mL being pumped through the wells. This time frame conveniently allowed the experiment to begin in the late afternoon, continue overnight and stop the next morning.

After 20 hours, the syringe was removed from the pump and the entire setup was transferred into the biosafety cabinet (KOJAIR, BioWizard Silver Line Biosafety cabinet). To replicate the conditions of the proton radiation experiment, where the chip must be placed vertically due to the horizontal orientation of the proton beam, the chip was also positioned vertically for one hour. This step checked for potential leakage.

Afterwards, fresh cell culture medium was inserted into the syringe and the whole setup was placed back inside the incubator. A flow rate was applied for an additional 2 hours.

Meanwhile, 20 µL of the output medium from the initial 20-hour flow rate was collected by first pipetting the medium up and down several times to ensure a homogeneous distribution of cells, as they tend to sink to the bottom of the tube, especially after long periods of stationary incubation. Afterwards, it was mixed with the viability dye, pipetted into a Countess slide and inserted into the Countess 3 Automated Cell Counter. This showed if cells may have detached from the ibidi chip during flow rate. Measuring the number of cells, the percentage of live vs. dead cells and their average size provides insight into the effect of continuous flow rate on cell adhesion and viability.

A step-by-step protocol for setting up this flow rate experiment can be found in Appendix A.2.

3.4. Experimental setup for irradiating the on-a-chip system

This section will describe how the radiation experiments were performed. It was chosen to irradiate both the 12-well plate and ibidi chip with photons and protons, with either 2 or 5 Gy.

3.4.1. Photon irradiation

The photon irradiation experiments were conduced at Reactor Institute Delft (RID) using an X-ray tube (YXLON, Y.TU 320-D03). In order to determine the exact dose rate, which was estimated to be 1.5 Gy/min, a dosimetric calibration was performed first. The tube voltage was set at 250 kV, the current at 15 mA, the focal distance at 5.5 cm and a 1 mm Copper (Cu) filter was used (to remove low energy X-rays). Furthermore, Gafchromic EBT3 film (PEO Medical) was used at a sample-source distance of 30 cm. This dosimetric film, which is an active substrate layer of approximately 30 μm thick, is covered with a clear polyester layer on both sides of 125 μm thick. When exposed to liquids (which happens in the calibration setup), only the edges of the film are slightly affected. The film is suitable for dose measurements between 1 and 20 Gy.

The calibration was performed using a Co-60 gamma radiation source (Nordion), which had a dose rate of 24.5 Gy/h on the day of the calibration. As the deposited dose increased, the green color of the film turned darker. Transmission values, which decreased with higher doses, were measured using a flatbed scanner (Epson Perfection V700 Photo). A calibration curve was developed using doses ranging from 1 to 8 Gy to find the relationship between dose and optical density (OD) of the film. Since the film's response depended slightly on the time interval between irradiation and scanning, it was recommended to scan the film within 1 to 8 hours after irradiation.

The transmission (T) was converted to net optical density ($\mathrm{OD_{Net}}$) through the following equation:

$$\mathrm{OD_{Net}} = \log(T_{\mathrm{unexposed}}) - \log(T_{\mathrm{exposed}}). \tag{3.1}$$

The calibration equation equals:

$$D(\mathrm{Gy}) = a \times \mathrm{e}^{b \times \mathrm{OD}}, \tag{3.2}$$

where a and b are constants, which were derived after plotting the calibration data in Excel.

It was chosen to irradiate the chip and the 12-well plate with a dose rate of 1.6 Gy/min. Since a dose rate of 1.5 Gy/min was achieved at a distance of 30 cm from the source, the chip and the 12-well plate containing the dosimetric film were irradiated at several distances, ranging from 27 to 34 cm with steps of 1 cm, between the cell monolayer and the X-ray source. Pieces of films were cut and placed inside the chip and 12-well plate and covered with 30 µL and 1.15 mL of water, respectively, to mimic the experimental setup during actual irradiations.

The irradiation time was 2 minutes, resulting in doses between 1 and 5 Gy depending on the distance. Film transmission was measured 2 hours and 15 minutes after irradiation.

Fig. 3.6 shows the full calibration setup. Fig. 3.6(a) shows the Co-60 source machine and Fig. 3.6(b) shows the dosimetric film placed inside a holder which goes into the Co-60 source machine, Fig. 3.6(c) shows the results from irradiating the dosimetric film with the Co-60 source and the X-ray source and Fig. 3.6(d) shows the dosimetric film placed inside the flatbed scanner.

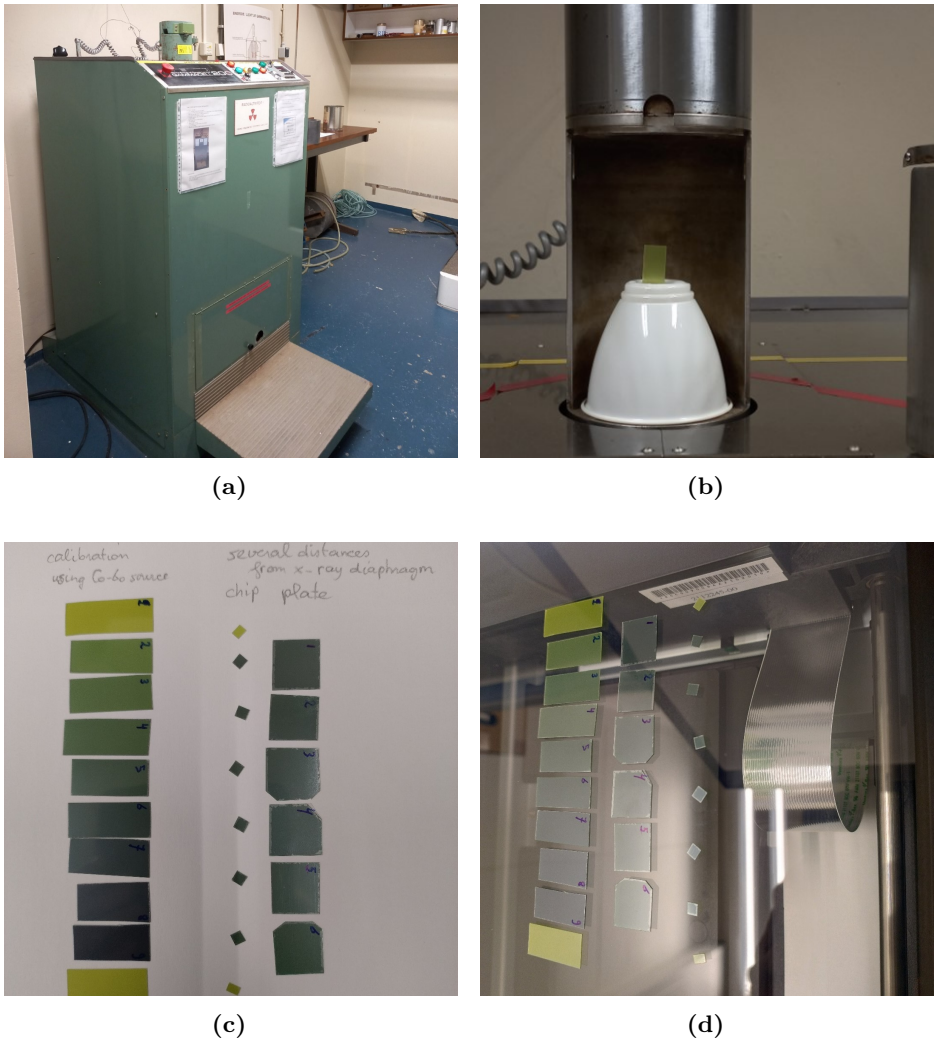

(a) **(b)**

(c) **(d)**

Figure 3.6: Complete experimental setup of the X-ray tube calibration with the Co-60 source, where (a) shows the Co-60 source machine, (b) the dosimetric film placed inside a holder, (c) the results of the dosimetric film after irradiations and (d) the dosimetric film placed inside the flatbed scanner

When the dose rate (Gy/min) as a function of distance (cm) was plotted, a linear relation was found and given by the equation:

$$R_x(\text{Gy/min}) = a \times x + b = a \times d(\text{cm}) + R_0(\text{Gy/min}), \tag{3.3}$$

where R_x equaled the desired dose rate (1.6 Gy/min), a equaled the slope of the linear plot (in Gy/cm) and R_0 equaled the actual dose rate. When this equation was rewritten, the distance d was expressed as:

$$d(cm) = \frac{(R_x - R_0)}{a}. \tag{3.4}$$

After the values for R_x, R_0 and a were filled in, the required distances to achieve a dose rate of 1.6 Gy/min were calculated to be 30.4 cm for the chip and 32.6 cm for the 12-well plate.

For the radiation experiments with the cells seeded on both the chip and the 12-well plate, the same X-ray settings, thus 250 kV, 15 mA and 5.5 cm focal distance, were used. In order to deliver 2 Gy, the exposure time was set to 1 minute and 40 seconds and for 5 Gy to 3 minutes and 8 seconds. The X-ray

source was oriented vertically, so the chip and the 12-well plate were positioned flat underneath the beam. Fig 3.7 shows the experimental setup for both the chip and the 12-well plate.

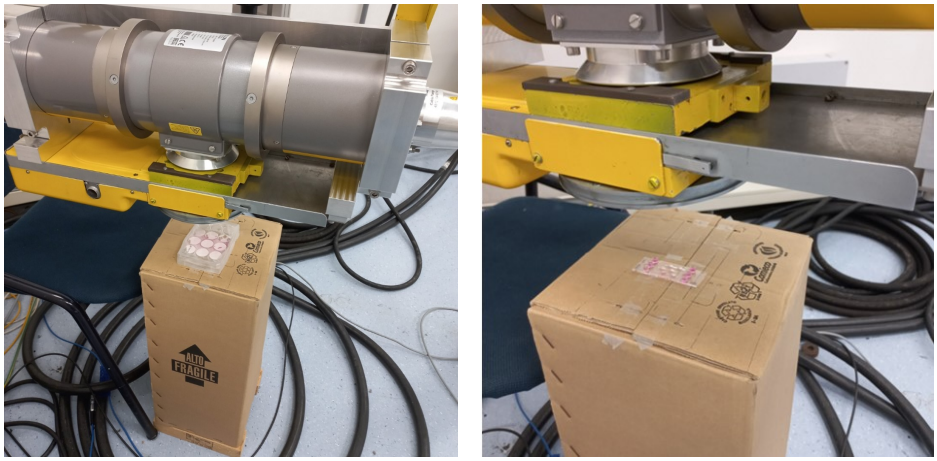

(a) **(b)**

Figure 3.7: Experimental setup for photon irradiation of the 12-well plate (a) and the ibidi chip (b) at RID

3.4.2. Proton irradiation

The proton irradiations were conducted at the Holland Proton Therapy Center (HollandPTC) in Delft, using the R&D proton beamline, which is horizontally orientated and can deliver energies ranging from 70 up to 240 MeV [60]. To generate a uniform dose distribution across the target, a 2D range modulator was used to create a spread-out Bragg peak (SOBP) of approximately 3 cm in depth. For the experiments, an energy of 150 MeV, a current of 800 nA and an the maximum irradiation field size of 8x8 cm^2 was used. As mentioned in Section 3.1, the delivered dose was either 2 or 5 Gy, with a dose rate of (6,62 Gy/min). Fig 3.8(a) shows a schematic drawing of the beam setup.

Before irradiating the 12-well plate, 1 mL of medium from each well containing a coverslip with seeded cells was removed, leaving approximately 150 µL medium behind. Additionally, the 1 mL PBS in the surrounding wells was removed as well. This step is necessary because the plate was positioned vertically during irradiation and if not removed, it could have lead to uneven coverage of the coverslip, which may have affected dose delivery.

Once the medium and PBS were removed, the 12-well plate was sealed with a PCR plate seal (Eppendorf, Cat.No: 0030127781), the lid replaced and the entire plate secured with Parafilm to prevent leakage, as seen in Fig. 3.8(b). Afterwards, the plate was positioned in the proton beamline setup, as seen in Fig. 3.8(c). After placing the plate correctly, the doors to the experimental room were closed and irradiation was started.

After irradiation, the previously removed medium and PBS were returned to their wells. After that, the 12-well plate was placed back into the incubator for 2 hours.

For the ibidi chip, the procedure was slightly different. After 20 hours of flow rate, the chip was removed from the incubator and the tubings disconnected. The reservoirs were then sealed with a piece of Parafilm to prevent leakage. Then, the chip was placed in front of the proton beamline, as seen in Fig. 3.8(d). Once the doors to the irradiation room were closed, irradiations were started.

Afterwards, the chip was reconnected to the tubings and the syringe filled with several mL of fresh culture medium. The setup was returned to the incubator and flow rate was applied for an additional 2 hours.

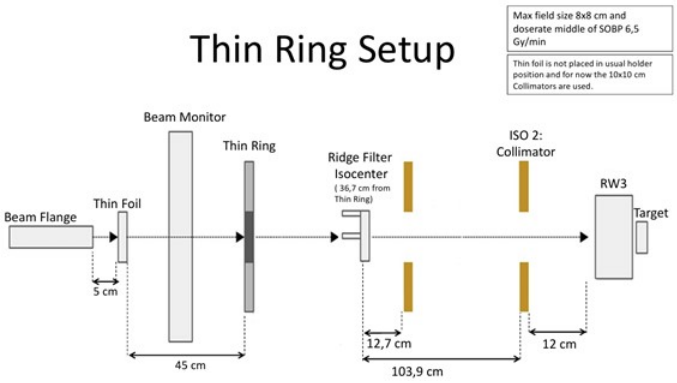

(a)

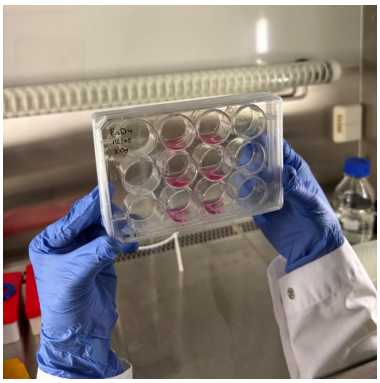

(b)

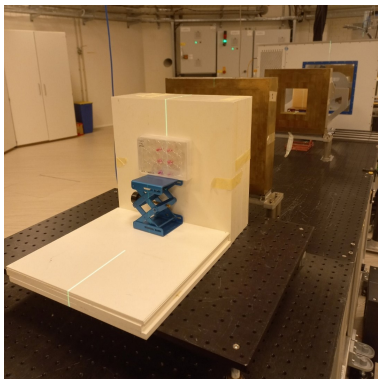

(c)

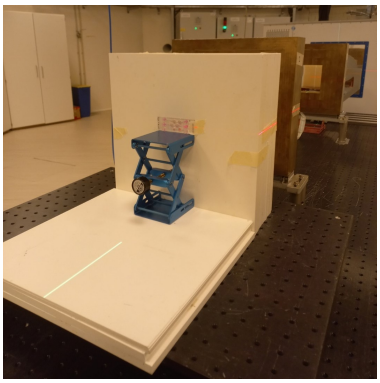

(d)

Figure 3.8: Experimental setup for proton irradiation (a) of the 12-well plate (b) and (c) and the ibidi chip (d)

3.5. Readouts

In order to assess whether the flow rate conditions were optimal, as well as reading out data from the radiation experiments, several markers were used. These include γ-H2AX, Ki-67, Phalloidin-TRITC and Hoechst 33258 and is either binded to a fluorophore, or already emitting a color. The assessment using this technique is called immunocytochemistry fluorescence. However, before these markers can be used, the cells need to be fixated first.

3.5.1. Fixation

For the 12-well plates, the cell culture medium was carefully removed from each well to avoid scratching the coverslip, as cells were attached to its surface. Each well was washed once with 1 mL PBS before adding 1 mL of a paraformaldehyde (PFA) solution. Cells were incubated in PFA for 5 minutes at room temperature, after which the solution was removed. Finally, 1 mL PBS was added to each well, and the plate was stored at 4°C until further use.

For the ibidi chips, fixation was performed using syringes, since the wells were sealed with a polymer coverslip. After disconnecting the tubing from the reservoirs, two 10 mL syringes were prepared: one containing 6 mL of PBS (at 37°C) and another containing 3 mL of cold PFA (4°C). The PBS-filled syringe was connected to the inlet reservoir, and 1 mL was slowly pushed through the channels while the chip was held at a slight angle above a cup. This process was repeated for all inlet reservoirs. The same procedure was then carried out with the PFA solution, which was incubated for 5 minutes at room temperature. Finally, the chip was flushed again with PBS and the reservoirs were filled with PBS before being sealed with Parafilm. The chip was stored at 4°C until further use.

The step-by-step protocol can be found in Appendix A.1.3.

3.5.2. Immunocytochemistry fluorescence

For the 12-well plates, cells were first permeabilized by removing PBS from the wells and adding 0.5 mL of 0.2% Triton X-100 in PBS for 15 minutes at room temperature. After removing the solution, the wells were washed once with 0.5 mL PBS. To block non-specific binding, 0.5 mL of 5% BSA in PBS was added and incubated for 30 minutes to 1 hour in a humid chamber at room temperature. Coverslips were then positioned upside down onto drops of primary antibody solution (γ-H2AX, Ki-67, diluted in 3% BSA/PBS) placed on a piece of labeled Parafilm. Incubation with the primary antibodies was carried out overnight at 4°C in a humid chamber.

The next day, the coverslips were returned to the wells and washed twice with PBS. Incubation was then performed with Phalloidin-TRITC and the secondary antibodies Alexa 488 and Alexa 647, each diluted (1:500) in 1% BSA/PBS, for 1 hour at room temperature in a dark humid chamber. After incubation, coverslips were washed twice with 0.5 mL PBS for 5 minutes each and counterstained with Hoechst 33258 (1:1000 dilution) for 5 minutes, followed by another PBS wash. Glass slides were cleaned with ethanol and labeled with experimental details, after which two drops (20 µL each) of Vectashield mounting medium were placed on the slide. Stained coverslips were mounted upside down on the medium and the slides were stored in a dark box at room temperature for 1 day before being wrapped in aluminum foil and stored at 4°C.

For the ibidi chips, the polymer coverslip was first removed and placed, with the sticky-side down, on aluminum foil. PBS was removed from the wells and reservoirs and 30 µL of 0.2% Triton X-100 in PBS was added to each well for 15 minutes at room temperature. The solution was then removed, followed by one wash with 30 µL PBS. Blocking was performed with 30 µL of 5% BSA in PBS for 30 minutes to 1 hour at room temperature in a humid chamber. Afterwards, 30 µL of the primary antibody solution (γ-H2AX, Ki-67 in 3% BSA/PBS) was added and the slide was incubated overnight at 4°C in a humid chamber.

On the second day, the primary antibody solution was removed and the blocking step was repeated. The wells were then incubated with Phalloidin-TRITC and secondary antibodies Alexa 488 and Alexa 647, diluted (1:500) in 1% BSA/PBS, for 1 hour at room temperature in a dark humid chamber. Afterwards, the wells were washed twice with 30 µL PBS for 5 minutes each, counterstained with Hoechst 33258 (1:1000 dilution) for 5 minutes and washed once more with PBS. Finally, the polymer coverslip was placed back on top of the wells, the chip was wrapped in aluminum foil and stored at 4°C.

The step-by-step protocol can be found in Appendix A.3.

Tables 3.2 and 3.3 give an overview of all antibodies and markers used, including their target, fluorophore, emission range, dilution and company where the markers and fluorophores have been bought. Appendix A.3 provides a step-by-step protocol for cell staining.

Table 3.2: Antibodies used to stain the FaDu cells after the experiments with their targets, fluorophores, emission range, dilutions and company where it was bought. When there are multiple dilutions given, the dilution before the slash is meant for the marker and after the slash for the fluorophore. The same applies for the company

1st Antibody	**Target**	**2nd Antibody**	**Emission (nm)**	**Dilution**	**Company**
γ-H2AX, rabbit, anti-human	DNA DSBs	Alexa Fluor 647, goat anti-rabbit	647 - 668	1:250–1:500 / 1:500	abcam (ab81299) / ThermoFisher
Ki-67, mouse, anti-human	Cell proliferation	Alexa Fluor 488, goat anti-mouse	488 - 517	1:200 / 1:500	Agilent (M724029-2) / ThermoFisher

Table 3.3: Markers used to stain the FaDu cells after the experiments with their targets, emission range, dilutions and company where it was bought

Marker	Target	Emission (nm)	Dilution	Company
Phalloidin-TRITC	Cytoskeleton	517	1:200–1:500	ThermoFisher (P1951)
Hoechst 33258	DNA / Nucleus	465	1:1000	Molecular Probes

3.5.3. Data acquisition

Data acquisition, including imaging and taking pictures of the samples after the conducted experiments, was done using the ZEISS LSM 980 upright confocal fluorescence microscope with Airyscan 2 detection and controlled via the ZEISS ZEN 3.12 (lite) software. Images were taken with a magnification of 20× (in air) and 40× (in oil) using Plan-Apochromat objectives with numerical apertures (NA) of 0.8 and 1.2, respectively. The fluorophores described in the previous section were excited with laser lines at 653 nm for Alexa Fluor 647 (AF647-T3), 493 nm for Alexa Fluor 488 and TRITC (AF488-T2 channel) and 353 nm for Hoechst 33258 (DAPI-T3 channel). For each sample and condition, at least three images were taken at random positions across the sample for all fluorescence channels.

3.5.4. Data analysis

For the data analysis, the pictures taken with the confocal fluorescence microscope were opened in ZEISS ZEN 3.12 (lite) software. A scale bar was added for every channel (50 µm for the 20× images and 20 µm for the 40× images). Screenshots were taken of every channel and pasted into a Word document. The width of every picture was set to 5 inch and saved as a PNG image. For the analysis it was important to know what the µm/pixel ratio was of the images to be able to convert pixels to micrometers. This was done in ImageJ by selecting the Straight Line Tool from the toolbar and drawing a line exactly over the length of the scale bar. After measuring, the length appears in pixels. The analysis was done with a custom Python script, in Jupyter Notebook (anaconda3) environment, or descriptive and is explained below for every staining.

Hoechst 33258

With the Python code the Hoechst images were analyzed to quantify the number and size of cell nuclei in each image.

The PNG saved screenshots were loaded and changed to a grayscale array. Next, the length of the scale bar and its corresponding pixel length measured in ImageJ was entered.

In order to reduce background noise, a Gaussian blur filter with a kernel size of 3x3 was applied. Next, to determine an intensity cutoff which separates foreground nuclei with background pixel, Otsu's method was used to perform this thresholding. Segmented objects that were smaller than e.g. 75 µm^2 or bigger than 1500 µm^2 were excluded, varying with magnification and type of sample.

To separate overlapping nuclei, a distance transform was computed on the binary mask, followed by watershed segmentation using a minimum distance in µm between the center of nuclei, varying with magnification and type of sample as well. This ensured that closely positioned nuclei were properly segmented as individual objects.

For each identified nucleus, the area (µm^2) and diameter (µm) were calculated from the segmented binary mask. The total number of nuclei per images, as well as the minimum, maximum and mean areas were derived. These results were saved to a CSV file, as well as the segmentation overlay images with red boundaries and numbered nuclei as a PNG file. Afterwards, the Standard Error of Mean (SEM) was calculated in Excel, by calculating the standard deviation of the total number of cells counted for one condition (e.g. images of the ibidi chip exposed to a flow rate with 20× magnification) and then divided by the square root of the total amount of images for that same condition. This was also calculated for the minimal, maximal and mean area in µm^2. Furthermore, the average was calculated for these parameters and conditions as well.

Table 3.4 gives an overview of the parameter values used in the custom made Python script for the

Hoechst image analysis. The complete Python script used for this analysis can be found in Appendix B.1, as well as a few example images produced by this Python code of the segmented Hoechst images with an overlay in Appendix B.2.

Table 3.4: Overview of Hoechst image analysis parameter values used in the custom made Python script for each sample and magnification

Sample	Staining	Mag.	Scale bar (µm)	Min area (µm^2)	Max area (µm^2)	Watershed distance (µm)
Coverslip	Hoechst	40×	20	100	1500	5
	Hoechst	20×	50	75	1500	15
Chip	Hoechst	40×	20	100	1500	15
	Hoechst	20×	50	200	1500	20

Ki-67

Another Python code was written to quantify the number of proliferating (Ki-67-positive) and non-proliferating (Ki-67-negative) cells in each image.

The PNG screenshots were loaded and converted to a grayscale array. The scale bar length and its pixel length measured in ImageJ were provided, varying with magnification and type of sample.

To reduce background noise, a Gaussian blur filter with a kernel size of 3x3 was applied. To determine the intensity threshold separating foreground nuclei from the background, Otsu's method was used. Objects smaller than e.g. 75 µm^2 or larger than 1500 µm^2 were excluded, also varying with magnification and type of sample.

To separate overlapping nuclei, a distance transform was computed on the binary mask, followed by watershed segmentation using a minimum distance between the centers of nuclei, given in µm. This ensured that closely located cells were correctly segmented as individual objects.

For each identified nucleus, the area (µm^2) and mean intensity were measured. Cells with a mean intensity value equal to or higher than e.g. 75 were classified as Ki-67-positive. The total number of cells, the number of Ki-67-positive and Ki-67-negative cells, and the fraction of Ki-67-positive cells per image were calculated. These results were saved to a CSV file, as well as the segmentation overlay images in which red boundaries indicated the segmented nuclei and green and red markers represented Ki-67-positive and Ki-67-negative cells, respectively.

Table 3.5 gives an overview of the parameter values used in the custom made Python script for the Ki-67 image analysis. The complete Python script used for this analysis can be found in Appendix B.3.

Table 3.5: Overview of Ki-67 image analysis parameter values used in the custom made Python script for each sample and magnification

Sample	Staining	Mag.	Scale bar (µm)	Min area (µm^2)	Max area (µm^2)	Watershed distance (µm)	Intensity threshold
Coverslip	Ki-67	40×	20	75	1500	5	70
	Ki-67	20×	50	75	1500	15	65
Chip	Ki-67	40×	20	150	1500	20	75
	Ki-67	20×	50	200	1500	20	70

Phalloidin-TRITC

The Phalloidin-TRITC images, which stained actin filament (F-actin), were categorized based on sample type (ibidi chip or coverslip) and magnification (20× or 40×). In contrast to the Hoechst and Ki-67 image analysis, these images were visual descriptively analyzed in terms of cell morphology, spatial distribution and clustering. This was done after the images were altered to a grayscale in Word to enhance contrast.

4

Results & Discussion

This chapter presents and analyzes the results obtained from the experiments described in the previous chapter. The data is organized by the staining markers used, starting with Phalloidin-TRITC, followed by Hoechst 33825, Ki-67 and γ-H2AX. In the next section, results will be discussed and recommendations for future research will be provided.

4.1. Image analysis

For every staining, a small introduction is provided, as well as several images that represent that average data. All images used for the data analysis can be found in the following folder in the TU Delft environment: M:/tnw/rrrrid/rrr/ari/ARI_data/Reports, theses and presentations/Stage en afstudeerverslagen/Milou Sengers MSc 2025/Data Milou

4.1.1. Phalloidin-TRITC

Phalloidin-TRITC is a fluorescent marker that binds to the filamentous actin (F-actin), which visualizes the cytoskeleton of the cell. It was used to analyze the cell's morphology and to determine whether flow rate has an effect on the shape of the cells. Image analysis was done through visual observation of cell morphology, spatial distribution and clustering.

Fig. 4.1 shows three grayscale fluorescence images which represent the average result of this staining, obtained with a magnification of 40×.

Fig. 4.1(a) shows coverslip-cultured cells irradiated with 5 Gy protons. The cells appear round with clear actin cytoskeleton due to contact with focal adhesions, are clustered closely together and show little spreading and have therefore compact spatial distribution.

In contrast, chip-cultured cells exposed to flow rate (400 µL/h), not to radiation, shown in Fig. 4.1(b), do not show clear focal adhesion, appear to have a more stretched out morphology and are more widely spaced, possibly due to the induced shear stress. This suggests that under flow rate conditions, cells spread out more and are less clustered together.

Fig. 4.1(c) shows chip-cultured cells without being exposed to either flow rate or radiation. These cells display a morphology more comparable to those in Fig. 4.1(a), remaining relatively round with focal adhesion, but their spatial distribution and clustering are more similar to the flow rate condition.

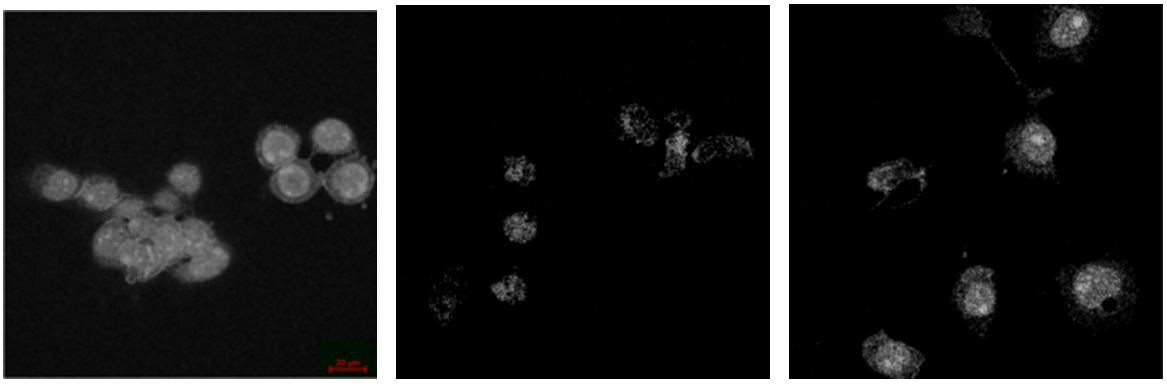

(a) (b) (c)

Figure 4.1: Phalloidin-TRITC-stained images obtained by a fluorescence microscope with a magnification of 40×, altered to a grayscale. (a) shows coverslip-cultured cells, exposed to 5 Gy proton radiation. (b) shows chip-cultured cells exposed to flow rate (400 µL/h), without radiation. (c) shows chip-cultured cells without both flow rate and radiation. The scale bar represents 20 µm and applies to all images

4.1.2. Hoechst 33825

Hoechst 33825 is a fluorescent dye that binds to DNA, which visualizes the cell's nucleus. This staining was used to clearly distinguish individual cells and to analyze cell count and mean nucleus area (µm^2), which could be enhanced by flow rate. Data analysis was done with a custom Python code. Since this staining has a good contrast resolution, it is also used to investigate cell's spatial distribution and clustering.

Effect of flow rate on number of cells under varying radiation conditions

Fig. 4.2 shows two fluorescence microscopy images of chip-cultured cells stained with Hoechst 33825, obtained with a magnification of 20×, which are close to the average data in terms of cell count. In figure (a), the cells were exposed to flow rate (400 µL/h) and no radiation. In figure (b), cells were not exposed to neither flow rate nor radiation. It shows that cells under flow rate conditions appear more clustered and less distributed compared to static condition, where cells are less clustered and more spatially distributed. The number of cells is less under flow rate conditions (3.2 ± 0.59) compared to static conditions (16.3 ± 4.0), as shown in the first two rows of Table 4.1.

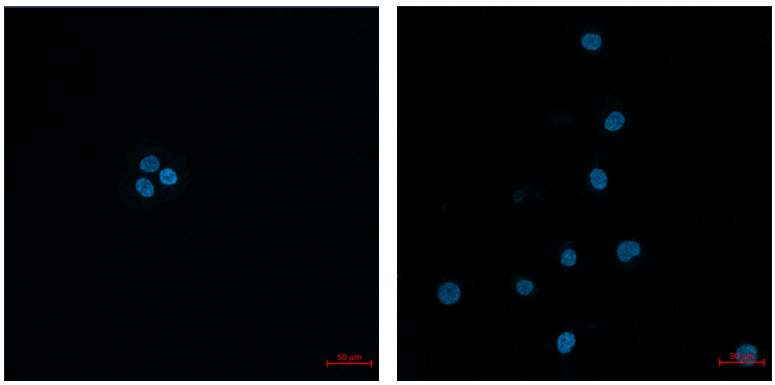

(a) (b)

Figure 4.2: Hoechst-stained images obtained by a fluorescence microscope with a magnification of 20×, where (a) shows chip-cultured cells exposed to a flow rate (400 µL/h), without radiation. (b) also shows chip-cultured cells, without a flow rate and radiation. The scale bar represents 50 µm

Fig. 4.3 shows fluorescence images of chip-cultured cells stained with Hoechst and imaged with a

magnification of 40×. In figure (a), cells were exposed to a flow rate (500 µL/h) and 5 Gy proton radiation, while in figure (b) cells received the same radiation type and dose but without a flow rate. The cells under flow rate conditions appear slightly fewer in number compared to the static condition. This finding is supported by the data in the lower two rows of Table 4.1, where the mean cell count under flow rate conditions (5.0 ± 0.97) was lower than under static conditions (7.3 ± 1.45). These results may suggest that flow rate reduces the number of cells attached to the chip and cell spreading behavior, both with and without being exposed to radiation.

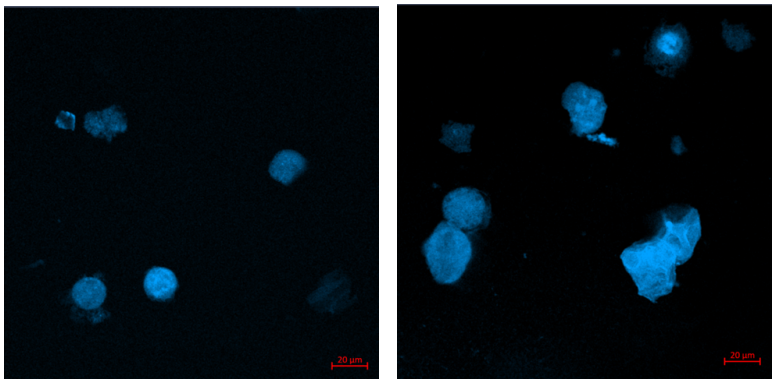

(a) **(b)**

Figure 4.3: Hoechst-stained images obtained by a fluorescence microscope with a magnification of 40×, where (a) shows chip-cultured cells exposed to a flow rate (500 µL/h) and 5 Gy proton radiation. (b) also shows chip-cultured cells irradiated with 5 Gy protons, but without a flow rate. The scale bar represents 20 µm

Table 4.1: Summary of mean cell count for chip samples under different magnification, radiation and flow rate conditions, obtained after image analysis of Hoechst-stained images with a custom Python code, where N is the number of images analyzed and the total cell count represents the number of cells identified across those N images

Sample	Mag.	N	Total cell count	Radiation	Dose (Gy)	Flow	Mean cell count ± SEM
Chip	20×	10	32	9 None, 1 Proton	0 & 5	Yes	3.2 ± 0.59
	20×	6	98	None	0	No	16.3 ± 4.0
	40×	6	30	Proton	5	Yes	5.0 ± 0.97
	40×	3	22	Proton	5	No	7.3 ± 1.45

In order to determine the statistical significance of the mean cell count difference between the chip-cultured cells exposed to a flow rate (400 µL/h) and without flow rate, where images were obtained with a magnification of 20×, a statistical analysis was performed, as shown in Fig. 4.4. This was a two-tailed, two-sample t-test assuming equal variances. It revealed a statistically significant difference between the two conditions ($p = 0.0012$, ** = $p < 0.01$). This result indicates that the presence of flow rate decreases the number of adherent cells within the wells of the chip.

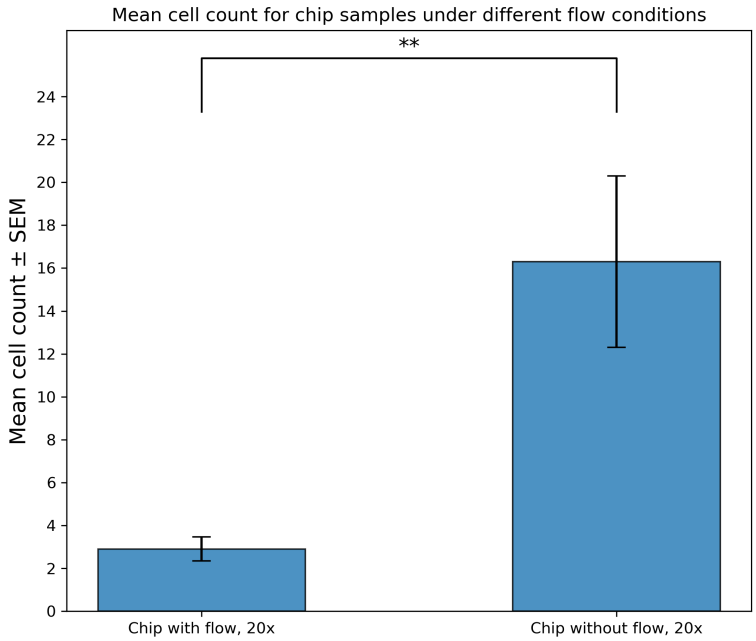

Figure 4.4: Comparison of mean cell count (± SEM) of cells cultured on chips under different flow rate conditions, imaged with a magnification of 20×. The one image where cells were exposed to 5 Gy proton radiation (see Table 4.1) was excluded to ensure comparable radiation conditions between the two samples. Statistical significance between groups is indicated (** = $p < 0.01$)

Table 4.2 summarizes the results of measuring the exit medium collected after flow rate and radiation experiments with the chip in terms of cell concentration (cells/mL), viability and average cell size (µm), obtained with the Countess 3 Automated Cell Counter. For the X-ray-irradiated samples, no cells are detected in the medium collected after exposure to both 2 and 5 Gy, while there are cells detected before irradiation. In contrast, the proton-irradiated samples show cell concentrations in the exit medium both before and after irradiation. Notably, the 5 Gy proton condition contains a higher cell concentration (1.57×10^4 cells/mL) after irradiation compared to the pre-irradiation sample (1.05×10^4 cells/mL). Furthermore, the average size of living cells is larger than that of dead cells across all conditions and an increase in both live and dead cell diameters is observed at higher radiation doses. These results may indicate that differences in radiation type and flow rate conditions contribute to cell detachment, which could explain the lower number of nuclei observed in the Hoechst-stained chip images under flow rate conditions.

Table 4.2: Overview of cell concentration, viability and size measurements in the exit medium from the chip (collected before and after irradiation) under the same flow rate condition (500 µL/h) but different radiation conditions, obtained with the Countess 3 Automated Cell Counter

Radiation	**Dose (Gy)**	**Medium collection**	**Cells/mL**	**Alive (%)**	**Dead (%)**	**Avg. alive cell size (µm)**	**Avg. dead cell size (µm)**
X-ray	2	Before	5.23×10^3	100	0	4.9	-
		After	0	-	-	-	-
	5	Before	2.09×10^4	75	25	6.86	7.66
		After	0	-	-	-	-
Proton	2	Before	1.05×10^4	50	50	3.69	7.36
		After	5.23×10^3	100	0	6.35	-
	5	Before	1.05×10^4	50	50	8.69	12.09
		After	1.57×10^4	67	33	9.92	11.02

Effect of radiation type on cell nucleus area under static conditions

Fig. 4.5 shows fluorescence images of coverslip-cultured cells irradiated with 5 Gy X-rays (a) and 5 Gy protons (b), both stained with Hoechst, under static conditions and imaged with a magnification of 40×. As shown in Table 4.3, the mean nucleus area is slightly larger for cells irradiated with X-rays (222.7 ± 13.3 µm^2) compared to cells irradiated with protons (207.5 ± 11.9 µm^2). This is also observed at 20× magnification, where the mean nucleus area is 331.5 ± 37.7 µm^2 for X-ray irradiation and 265.6 ± 27.1 µm^2 for proton irradiation. These results suggest that the nuclei of cells irradiated with X-rays tend to appear slightly larger on average than those irradiated with protons.

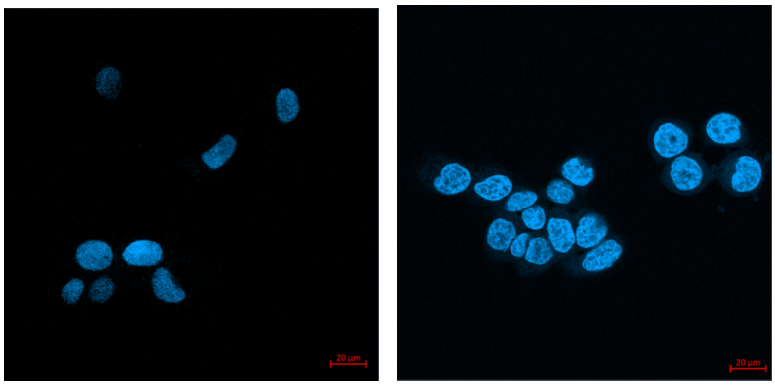

(a) **(b)**

Figure 4.5: Hoechst-stained images obtained by a fluorescence microscope with a magnification of 40×. (a) and (b) show coverslip-cultured cells irradiated with 5 Gy X-rays and 5 Gy protons, respectively. The scale bar represents 20 µm

Table 4.3: Summary of mean nucleus area for coverslip samples under different radiation conditions, obtained after image analysis of Hoechst-stained images with a custom Python code, where N is the number of images analyzed and the total cell count represents the number of cells identified across those N images

Sample	Mag.	*N*	Total cell count	Radiation	Dose (Gy)	Mean nucleus area ± SEM (µm^2)
Coverslip	20×	5	193	Proton	5	265.6 ± 27.1
	20×	5	70	X-ray	5	331.5 ± 37.7
	40×	10	129	Proton	5	207.5 ± 11.9
	40×	4	35	X-ray	5	222.7 ± 13.3

To evaluate whether radiation type influences the cell's nucleus size in static coverslip cultures, the mean nucleus areas of cells exposed to 5 Gy proton or X-ray radiation were compared, which were imaged with a magnification of 20× and 40×, as shown in Fig. 4.6. A two-tailed, two-sample t-test assuming equal variances was performed. It revealed a statistically significant difference between the two radiation types at both magnifications (20×: $p = 0.0046$, ** = $p < 0.01$ and 40×: $p = 0.0416$, * = $p < 0.05$). These findings suggest that proton radiation may cause smaller nucleus area compared to X-ray radiation.

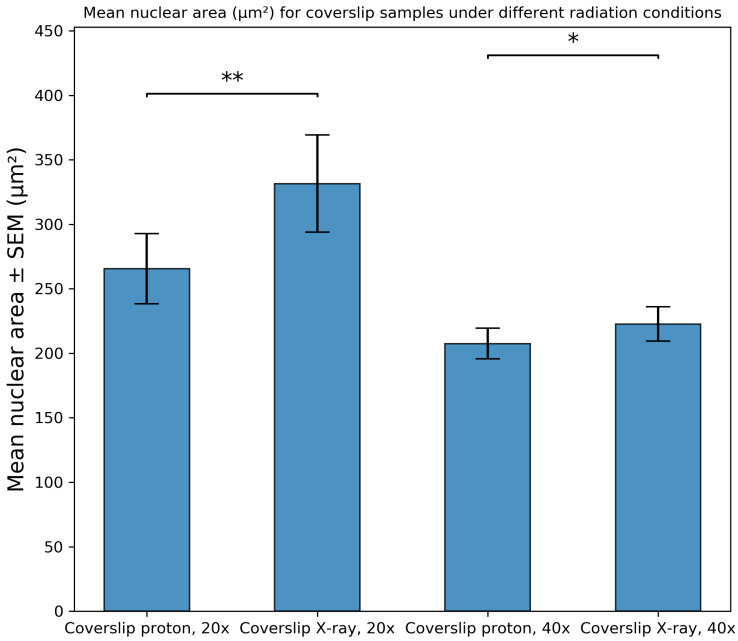

Figure 4.6: Comparison of mean nucleus area (± SEM) of cells cultured on coverslips and exposed to 5 Gy proton or X-ray radiation, imaged with a magnification of 20× or 40×. Statistical significance between groups is indicated (* = $p < 0.05$, ** = $p < 0.01$)

Effect of flow rate on cell nucleus area after proton radiation

Fig. 4.7 shows Hoechst-stained fluorescence images of coverslip- and chip-cultured cells irradiated with 5 Gy protons, imaged at a magnification of 40×. The data in Table 4.4 summarizes the mean nucleus area after image analysis with a custom Python code. Chip-cultured cells exposed to a flow rate (500 µL/h) exhibit a mean nucleus area of 350.4 ± 50.4 µm^2, while cells cultured under static conditions (no flow rate) show a slightly larger mean area of 400.6 ± 56.9 µm^2. In contrast, coverslip-cultured cells irradiated under the same proton conditions show smaller nuclei with an average area of 207.5 ± 11.9 µm^2 and cells irradiated with 5 Gy X-rays have a comparable mean nucleus area of 222.7 ± 13.3 µm^2. These results suggest that cells cultured on chips generally have a larger nucleus area, both under flow rate and static conditions, compared to coverslip-cultured cells, regardless of radiation type.

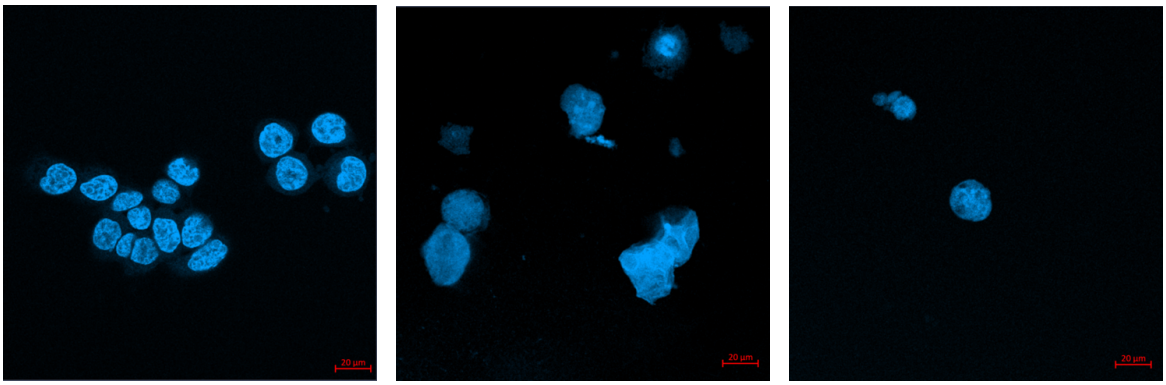

(a) **(b)** **(c)**

Figure 4.7: Hoechst-stained images obtained by a fluorescence microscope with a magnification of 40×, where (a) shows coverslip-cultured cells irradiated with 5 Gy protons. (b) shows chip-cultured cells irradiated with 5 Gy protons and without flow rate. (c) shows chip-cultured cells exposed to a flow rate (500 µL/h) and 5 Gy proton radiation. The scale bar represents 20 µm

Table 4.4: Summary of mean nucleus area for chip and coverslip samples under different flow rate conditions, but identical radiation conditions and magnification (40×), obtained after image analysis of Hoechst-stained images with a custom Python code, where N is the number of images analyzed and the total cell count represents the number of cells identified across those N images

Sample	Mag.	N	Total cell count	Radiation	Dose (Gy)	Flow	Mean nucleus area ± SEM (µm^2)
Chip	40×	6	30	Proton	5	Yes	350.4 ± 50.4
	40×	3	22	Proton	5	No	400.6 ± 56.9
Coverslip	40×	10	129	Proton	5	No	207.5 ± 11.9

To evaluate the effect of flow rate on nucleus size, the mean nucleus areas of chip-cultured cells with (500 µL/h) and without flow rate were compared to those of coverslip-cultured cells, all exposed to 5 Gy proton radiation and imaged with a magnification of 40×, as shown in Fig. 4.8. This was obtained using two-tailed, two-sample t-tests assuming unequal variances for comparisons between chip- and coverslip-cultured samples and equal variances for the comparison between chip conditions. It revealed a statistically significant difference between the chip without flow rate and coverslip samples ($p = 0.0038$, ** = $p < 0.01$), as well as between the chip exposed to a flow rate and coverslip samples ($p = 0.0116$, * = $p < 0.05$). In contrast, no significant difference was observed between chip-cultured cells with and without a flow rate ($p = 0.5744$). These findings suggest that the nucleus area is larger for chip-cultured cells compared to conventional coverslip-cultured cells, regardless of flow rate.

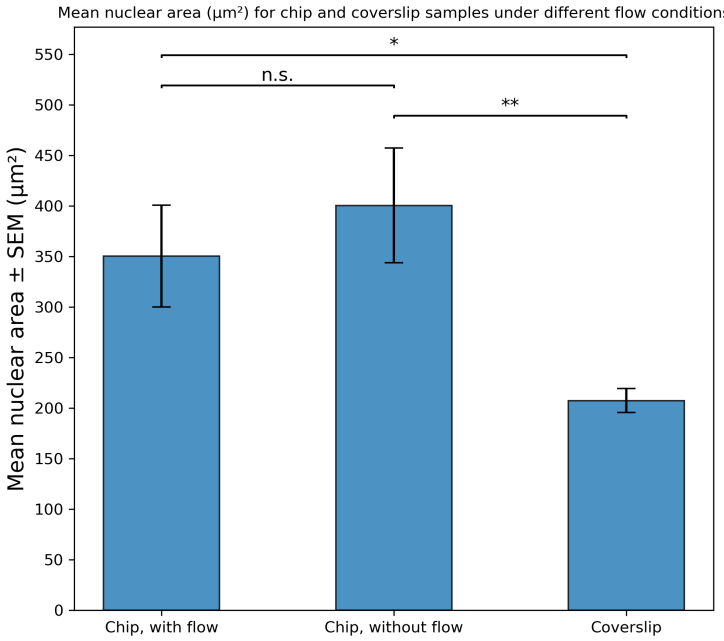

Figure 4.8: Comparison of mean nucleus area (± SEM) of cells cultured on chip exposed to a flow rate, on chip not exposed to a flow rate and on coverslips, exposed to 5 Gy proton radiation and imaged with a magnification of 40×. Statistical significance between groups is indicated (n.s. = not significant, * = $p < 0.05$, ** = $p < 0.01$)

4.1.3. Ki-67

Ki-67 is a fluorescence marker that targets a protein which is expressed when cells are proliferating, emitting a green color. It was used to determine whether cells continued to proliferate under flow rate conditions, which is a marker for cell viability and health. Data analysis was performed using a custom Python code to quantify the percentage of Ki-67+ (proliferating) cells in each image.

Effect of radiation type on Ki-67+ cells under static conditions

Fig. 4.9 shows fluorescence microscope images of coverslip-cultured cells stained for Ki-67 marker, which indicates cells are actively proliferating. Images (a) and (b) show coverslip-cultured cells samples irradiated with 5 Gy X-rays and 5 Gy protons, respectively, both under static conditions. The Ki-67 staining appears as green fluorescence within the nuclei of proliferating cells. Table 4.5 summarizes the percentage of Ki-67–positive cells obtained after image analysis with a custom Python code. For proton-irradiated samples, 47% of the cells are identified as Ki-67+, whereas X-ray–irradiated samples show a slightly lower percentage of 36%. These results suggest that proton-irradiated cells have a higher proliferative activity compared to those exposed to X-rays under otherwise identical conditions.

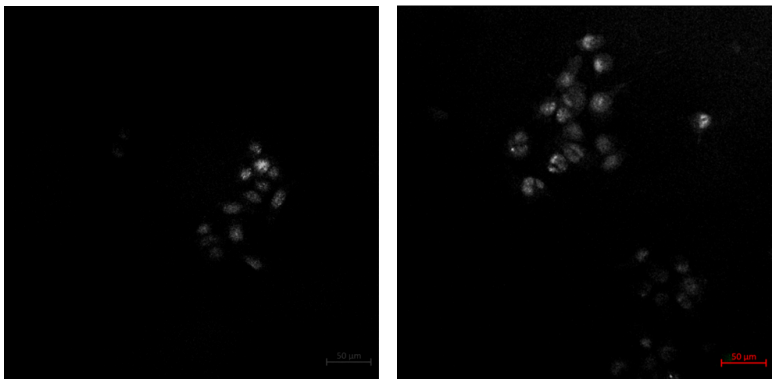

(a) **(b)**

Figure 4.9: Ki-67-stained images obtained by a fluorescence microscope with a magnification of 20×, altered to a grayscale, where both images are coverslip-cultured cells irradiated with 5 Gy X-rays and protons, respectively. The scale bar represents 50 µm and applies to both images

Table 4.5: Overview of Ki-67+ cell percentages for coverslip samples after 5 Gy radiation with either protons or X-rays, imaged with a magnification of 20×, obtained after image analysis of Ki-67 stained images with a custom Python code, where N is the number of images analyzed and the total cell count represents the number of cells identified across those N images

Sample	**Mag.**	***N***	**Total cell count**	**Radiation**	**Dose (Gy)**	**Ki-67+ ± SEM (%)**
Coverslip	20×	5	165	Proton	5	47 ± 14
	20×	5	47	X-ray	5	36 ± 18

To evaluate the effect of radiation type on cell proliferation, the percentage of Ki-67+ nuclei was compared between coverslip-cultured cells exposed to 5 Gy of either proton or X-ray radiation, based on images obtained with a magnification of 20×, as shown in Fig. 4.10. A one-tailed, two-sample t-test assuming equal variances was performed. It revealed no statistically significant difference between the two radiation types ($p = 0.3188$). These results suggest that there is little to no difference in proliferation response between the two radiation types.

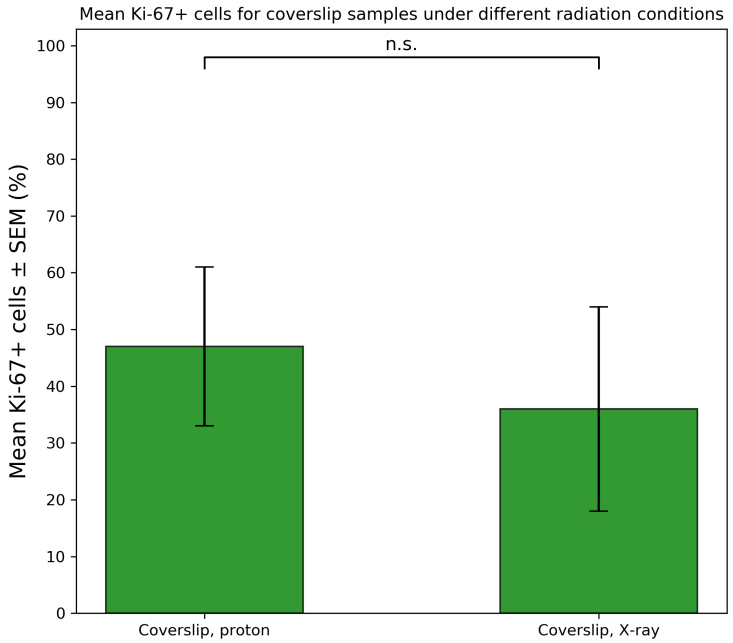

Figure 4.10: Comparison of mean percentage of Ki-67+ cells (± SEM) cultured on coverslips and exposed to 5 Gy proton or X-ray radiation, imaged with a magnification of 20×. Statistical significance between groups is indicated (n.s. = not significant)

Effect of flow rate on Ki-67+ cells after proton radiation

Fig. 4.11 shows fluorescence microscope images of Ki-67-stained cells to visualize cell proliferation after exposure to 5 Gy proton radiation under different culture and flow rate conditions. Images (a) and (b) display chip-cultured cells exposed to a flow rate (500 µL/h), imaged with magnifications of 20× and 40×, respectively, while (c) shows chip-cultured cells irradiated with 5 Gy protons, but under static conditions. Images (d) and (e) show coverslip-cultured cells under static conditions, also irradiated with 5 Gy protons and imaged with 40× and 20× magnification, respectively. The Ki-67 fluorescence signal is observed across all samples but appears brighter in chip-cultured cells compared to coverslip-cultured cells.

The data in Table 4.6 confirm these visual observations. Under flow rate conditions, chip-cultured cells show high Ki-67+ cells, with 100% at 20x and 88% at 40x magnification. In comparison, static chip-cultured cells also exhibit high proliferation (100%), while coverslip-cultured cells showed a lower percentage of Ki-67+ cells (47%) under both magnifications.

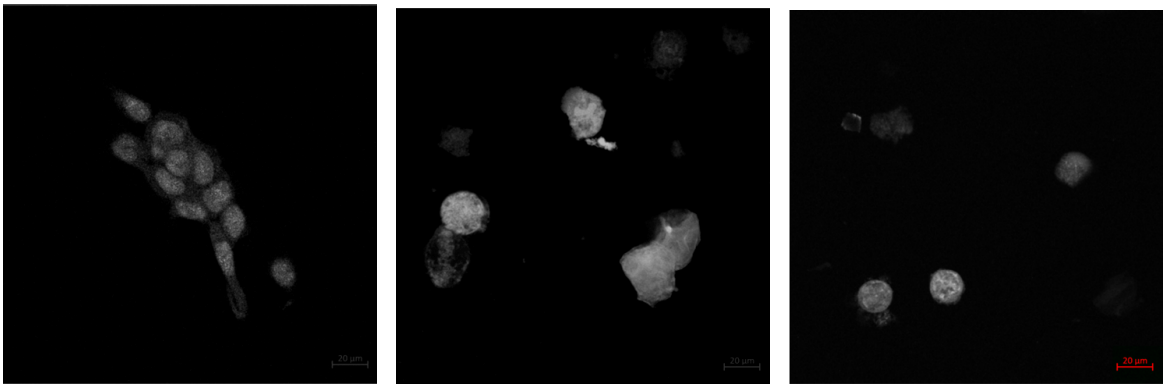

(a) **(b)** **(c)**

Figure 4.11: Ki-67-stained images obtained by a fluorescence microscope with a magnification of 40×, altered to a grayscale. (a) shows coverslip-cultured cells exposed to 5 Gy proton radiation, under static conditions. (b) shows chip-cultured cells exposed to 5 Gy proton radiation, but not to flow rate. (c) shows chip-cultured cells exposed to a flow rate (500 µL/h) and 5 Gy proton radiation. The scale bar represent 20 µm and applies to all images

Table 4.6: Overview of Ki-67+ cell percentages for chip and coverslip samples for different magnifications and flow rate conditions after 5 Gy proton radiation, obtained after image analysis of Ki-67 stained images with a custom Python code, where N is the number of images analyzed and the total cell count represents the number of cells identified across those N images

Sample	**Mag.**	***N***	**Total cell count**	**Radiation**	**Dose (Gy)**	**Flow**	**Ki-67+ ± SEM (%)**
Chip	20×	1	9	Proton	5	Yes	100
	40×	6	23	Proton	5	Yes	88 ± 13
	40×	1	4	Proton	5	No	100
Coverslip	40×	7	84	Proton	5	No	47 ± 17

To evaluate the effect of flow rate on cell proliferation, the percentage of Ki-67+ nuclei was compared between chip-cultured cells exposed to a flow rate (500 µL/h) and coverslip-cultured cells, both irradiated with 5 Gy protons and imaged with a magnification of 40×, as shown in Fig. 4.12. A one-tailed, two-sample t-test assuming equal variances was performed. It revealed a statistically significant difference between the two conditions ($p = 0.0486$, $* = p < 0.05$). These results suggest that flow rate enhances cell proliferation compared to static conventional coverslip cultures.

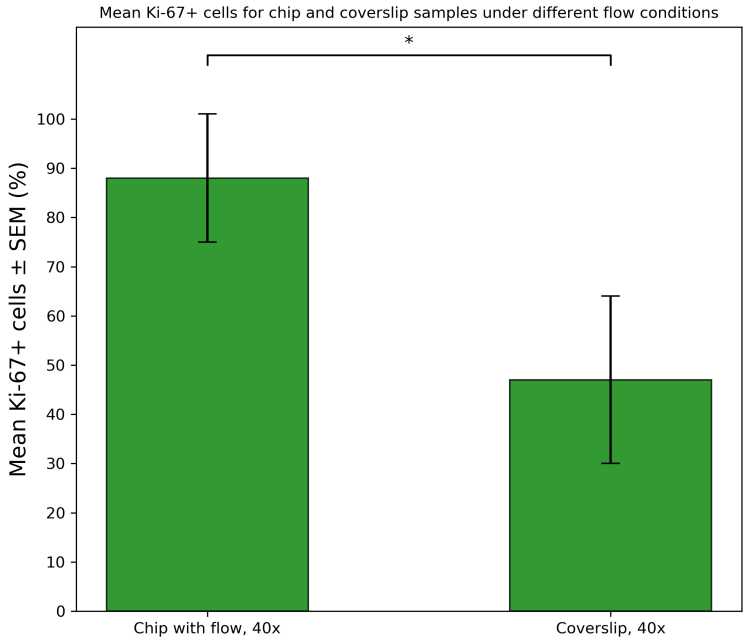

Figure 4.12: Comparison of mean percentage of Ki-67+ cells (± SEM) cultured on chip (under flow rate conditions) and coverslips, exposed to 5 Gy proton radiation, imaged with a magnification of 40×. Statistical significance between groups is indicated (* = $p < 0.05$)

4.1.4. γ-H2AX

γ-H2AX is a fluorescence marker which binds to a protein that releases when DNA damage (double-strand breaks) occurs in a cell. This could be caused by radiation exposure and when present, it emits a far-red color and appears as bright dots (foci) within the nuclei. This marker was initially used to compare radiation-induced DNA damage between X-ray and proton irradiation under flow rate conditions.

Fig. 4.13 shows fluorescence microscopy images visualizing DNA double-strand breaks (DSBs) using 53BP1 staining after 5 Gy X-ray and proton irradiation, obtained by Tim et al. [61]. Both figures show clear examples of 53BP1 foci forming in FaDu cell nuclei four hours after irradiation with 5 Gy X-rays (a) and protons (b). The bright white foci show the presence of DSBs, while the red and yellow circles show EdU+ (replicating) and EdU- (non-replicating) nuclei.

In contrast, the γ-H2AX-stained images obtained in this project through fluorescence microscopy with a magnification of 40× and altered to grayscale images, shown in Fig. 4.14, do not show as visible foci or fluorescent spots (which correspond to DNA damage) as clearly as in Fig. 4.13. Instead, the nuclei are mostly uniformly stained. This is clearly visible in figures (c) and (d), which are both images from chip-cultured cells irradiated with 5 Gy protons, under a flow rate (500 µL/h) and without flow rate, respectively. Figures (a) and (b), which are both images from coverslip-cultured cells irradiated with 5 Gy X-rays and protons, respectively, appear to show slightly more (potentially) foci formation. However, the signal remains too vague for it to be used for quantitative image analysis.

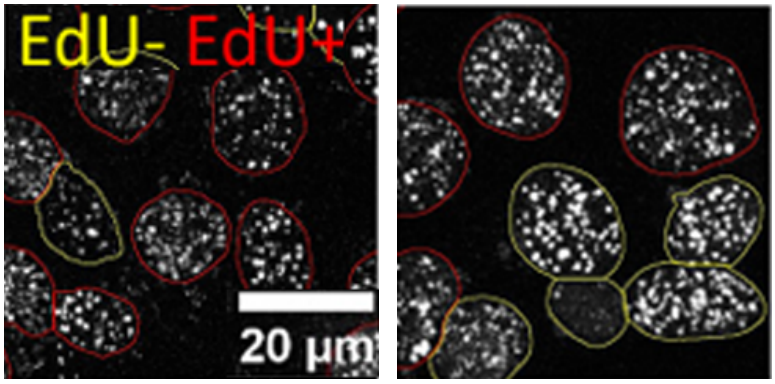

(a) (b)

Figure 4.13: 53BP1-stained images from [61] to visualize DSBs in FaDu cells, visible as bright white foci, 4 hours after 5 Gy X-ray (a) and proton (b) irradiation. EdU- and EdU+ nuclei, representing non-replicating and DNA-replicating cells, are also indicated by yellow and red circles, respectively [61]

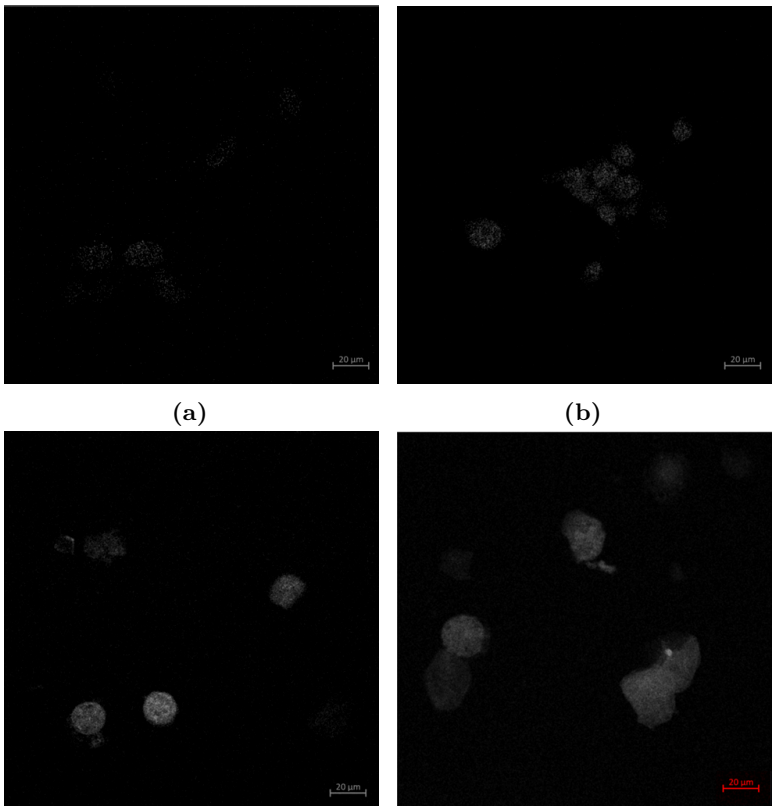

(a) (b)

(c) (d)

Figure 4.14: γ-H2AX-stained images obtained by a fluorescence microscope where (a) and (b) show coverslip-cultured cells irradiated with 5 Gy X-rays and protons, respectively. (c) and (d) show chip-cultured cells irradiated with 5 Gy protons under a flow rate (500 µL/h) and without flow rate, respectively. All images were imaged with a magnification of 40× and altered to a grayscale. The scale bar represents 20 µm

4.2. Discussion

This section discusses the results described in the previous section, as well as experimental challenges and data analysis limitations encountered during and after the experiments. It ends with several recommendations for future research.

4.2.1. Image analysis

Phalloidin-TRITC

The Phalloidin-TRITC images (Fig. 4.1) indicate clear morphological differences between coverslip-cultured cells exposed to 5 Gy proton radiation (a) and chip-cultured cells under either flow rate or static conditions ((b) and (c)), without radiation. The irradiated coverslip-cultured cells appear more rounded with well-defined cytoskeletal (actin) outlines, whereas chip-cultured cells, especially under flow rate conditions, show a more irregular and spread morphology. As discussed in Section 2.4, shear stress generated by continuous flow rate against the cell surface can influence cell morphology and cell layer organization, which likely explains the morphological changes observed in chip-cultured cells exposed to flow rate. Moreover, chip-cultured cells under static conditions still differ from coverslip cultures in terms of cell morphology, but the difference is less extreme than under a flow rate. This suggests that the environment of the chip, such as material, geometry and oxygen gradients, influences cell morphology, even without a flow rate.

Because cell fixation occurred already 2 hours after irradiation, major radiation-induced cytoskeletal changes were not expected, since most changes, after exposure to ionizing radiation, occurs after more than 2 hours (such as 4, 8 and 24 hours) [62]. Therefore, the observed differences are likely due to different culture conditions (coverslip vs. chip, flow rate vs. static) rather than radiation within this short time-frame after irradiation.

All images were obtained with a magnification of 40×, resulting in a limited number of cells per field of view. A larger sample size, which can be achieved by using lower magnification (20×) or imaging multiple fields within the sample, would improve the accuracy of these morphological findings.

Furthermore, during Phalloidin-TRITC imaging, the signal appeared green instead of red because it was detected using the 493 nm excitation channel instead of the correct TRITC excitation channel, which is approximately 544 nm. In order to enhance the contrast and visibility of the images, they were converted to a grayscale. However, the fluorescence color shift might have affected the signal intensity of the images and therefore the data outcome and interpretation. Follow-up experiments need to be performed to determine if this shift was possibly caused by the dye or imaging parameters.

Hoechst 33825

Effect of flow rate on number of cells under varying radiation conditions

Hoechst staining was used to examine whether flow rate influenced the number of adherent cells in the chip. For both magnifications and radiation doses, cell numbers were consistently lower under flow rate than under static conditions (Table 4.1). Statistical analysis further confirmed that flow rate significantly reduced the number of cells that remained attached (Fig. 4.4). This supports the explanation that shear stress, or other flow rate-induced changes in cell adhesion, contributes to detachment of cells from the chip surface. The analysis of the exit medium (Table 4.2) supports this interpretation by confirming the presence of large numbers of alive and dead cells washed away during flow rate. These findings indicate that the loss of adherent cells in the chip is due to flow rate.

Representative mean cell count Hoechst-stained images (Fig. 4.2) show how flow rate not only reduces cell attachment, but also changes spatial distribution. Cells under flow rate conditions were more clustered, while static cultures were more evenly spread. This suggests that cells may also be restricted in where they remain attached, causing them to accumulate in small regions.

Importantly, because cells were detached and washed away by flow rate, the total number of cells counted was not a reliable indicator of cell viability within the chip compared to the conventional coverslip experiments. However, analyzing the exit medium for cell count, size and viability does provide useful information about how well cells attach to the wells under flow rate conditions.

These results show that there is a trade-off of on-a-chip systems: while flow rate improves nutrient and oxygen supply, it also generates shear stress that can influence cell adhesion, morphology and cell layer

reorganization (as also discussed in Section 2.4).

Effect of radiation type on cell nucleus area under static conditions

To evaluate whether radiation type influences nuclear morphology in static coverslip cultures, the mean nucleus area of cells exposed to 5 Gy proton or X-ray radiation was compared using Hoechst-stained images obtained with a magnification of 20× and 40×. At both magnifications, X-ray–irradiated cells show significantly larger nuclei compared to proton-irradiated cells (Table 4.3 and Fig. 4.6). This pattern suggests that the two radiation modalities may induce different early nuclear changes or levels of DNA damage that results into measurable differences in nucleus size shortly after irradiation. Because nucleus area can reflect cell-cycle phase (with smaller nuclei typically reflecting G0/G1 phase and larger nuclei S or G2/M phase, see Fig. 2.5), differences in nucleus size may reflect changes in the distribution of cells being in a different cell-cycle phase. This may indicate that X-ray and proton irradiation induce the cells to change their cell cycle, which is important because radiosensitivity changes with cell-cycle phase.

A difference in measured nucleus area was also observed between 20× and 40× images under the same irradiation conditions. This is likely due to sampling differences (total cell count). At 20×, more cells were included in the analysis compared to 40× (193 vs. 129 for proton and 70 vs. 35 for X-ray, respectively). This increases the variability and sensitivity to outliers. Additionally, differences in pixel resolution and segmentation accuracy between magnifications may contribute to the differences in measured cell nucleus area.

Effect of flow rate on cell nucleus area after proton radiation

The analysis of nucleus area in proton-irradiated cells, imaged with a magnification of 40×, showed clear differences between chip-cultured and coverslip-cultured samples (Table 4.4). Specifically, chip-cultured cells showed larger nucleus areas than coverslip cultures, regardless of whether a flow rate was applied. This suggests that the chip environment itself, such as its geometry, material properties and applied mechanical forces, influences nuclear morphology after irradiation. Since nucleus size is related to cell-cycle phase, these differences may indicate that the chip environment changes the cell's cell-cycle distribution, which in turn could influence how the cells respond to radiation.

This idea is supported by the data in Table 4.2, which shows the sizes of live and dead chip-cultured cells collected from the exit medium after flow rate. This shows that the average size of dead cells is consistently larger than that of live cells and that the average cell size of both live and dead cells increases after radiation. This could indicate that many of the detached, non-viable cells were in the G2/M phase, which is characterized by larger nuclei and increased radiosensitivity.

Moreover, the average cell size also consistently increased after proton irradiation with 2 and 5 Gy, as shown in Table 4.2, which might be due to the 2 hour additional flow rate. However, these measurements have only been executed once and should be executed at least three times to increase its reliability.

A statistically significant difference was found between chip cultures under flow rate and coverslip cultures. This supports the idea that shear stress does not only affect cell adhesion (as shown in previous subsections), but may also influence cell morphology in irradiated cells.

Interestingly, no significant difference in nucleus area was observed between chip-cultured cells with and without flow rate. This suggests that flow rate may not further change nuclear morphology past the standard effect induced by the chip's environment due to its different (better) material properties compared to coverslips. The similarity between the two chip conditions could also be influenced by the low number of cells available for analysis, especially in the flow rate samples where many cells detached. With fewer cells left in the chip, the measurements may mainly reflect the nuclei of cells that were strong enough to stay attached. This means the results might be biased toward a small, more resilient cell population.

The visual comparison of representative images (in terms of cell nucleus area) from coverslips and chip cultures (Fig. 4.3) supports these findings. Nuclei of chip-cultured cells ((b) and (c)) appear larger and less uniform, whereas coverslip cultures (a) show more compact and regularly shaped nuclei.

Overall, these findings show that flow rate alone does not affect the cell's nucleus size after proton exposure, but the chip environment also changes nuclear morphology compared to conventional coverslip

cultures.

Ki-67

Effect of radiation type on Ki-67+ cells under static conditions

The Ki-67 analysis showed that both X-ray– and proton-irradiated coverslip samples contained a notable fraction of proliferating cells two hours after being irradiated with 5 Gy. The mean Ki-67+ percentage appeared higher in proton-irradiated samples (47%) compared to X-ray-irradiated samples (36%). However, the statistical analysis showed no significant difference. This suggests that the difference in means is likely due to sample variability than because of radiation-dependent biological effects.

The absence of a clear difference between X-rays and protons at this early time point is possible. Ki-67 shows cell-cycle activity, so changes in proliferation often occur several hours to days after irradiation as cells undergo cell-cycle arrest (G1 or G2 checkpoints), repair, or cell death signaling. At two hours after irradiation, many cells may not yet have completed a full cell-cycle, which means that early Ki-67 measurements show only very quick radiation-induced responses and could underestimate differences between radiation types that could occur later.

The relatively small number of analyzed images and total cell counts, especially of the samples irradiated with X-rays, may also add to variability in Ki-67+ percentages. Segmentation challenges, especially in clustered regions or areas with weak staining, may have added variability in the outcomes as well.

Overall, these results indicate that within the first two hours after exposure, proton and X-ray irradiation show similar proliferation responses in the coverslip samples. Future studies with larger sample sizes, better segmentation and additional time points (fixating the cells later after irradiation) would help determine if differences in proliferation activity do occur later, since radiation responses will become more noticeable then.

Effect of flow rate on Ki-67+ cells after proton radiation

The Ki-67 analysis showed that chip-cultured cells exposed to flow rate present a significant higher proliferation fraction compared to coverslip-cultured cells under static conditions after proton irradiation. The statistically significant difference between these two conditions suggests that the chip environment supports higher proliferation activity. This is in line with the idea that flow rate provides a more physiologically relevant environment by improving nutrient and oxygen delivery, as well as removing waste. Such conditions can help support the ongoing cell-cycle even after radiation, leading to a larger percentage of Ki-67+ cells.

Interestingly, chip-cultured cells under static conditions showed similar high Ki-67+ percentages as the cells under flow rate conditions. This suggests that the chip environment itself, independent of flow rate, may already help in obtaining higher proliferation activity compared to conventional coverslips. This could be due to the coating (ibiTreat) on the well's surface, which enhances cell's viability. Moreover, the polymer coverslip (placed over the wells) is gas-permeable, which allows for better oxygen and CO_2 diffusion, as well as preventing evaporation of culture media.

However, these conclusions are drawn with very small number of analyzed chip-cultured cells, especially under static conditions. This limits the ability to detect variability. Additionally, segmentation performance in small, densely packed chip regions may add uncertainty in identifying true Ki-67+ nuclei. While these limitations do not deny the observed trend, they suggest that the effects related to flow rate should be interpreted with caution.

Overall, the findings indicate that the chip culture environment, both with and without flow rate, supports higher proliferative activity after proton radiation compared to coverslip cultures.

γ-H2AX

The γ-H2AX staining did not result in clear DNA damage foci in any of the experimental conditions, despite the use of 5 Gy X-ray and proton radiation. In contrast, published data such as the 53BP1 images from Tim et al. [61] (Fig 4.13) show distinct and bright foci four hours after 5 Gy X-ray and proton irradiation of FaDu cells, showing the typical results of radiation-induced DSB markers. The absence of similar clear γ-H2AX foci in this project (Fig. 4.14) suggests that technical factors played a bigger role than biological differences between radiation types or culture platforms.

Future experiments should test different fixation times and γ-H2AX antibodies or 53BP1 staining, and use confocal microscopy to improve foci detection. Including controls, such as known DSB inducers or using protocols that have been validated, might help determine if these issues result from methodological problems or from biological variability.

4.2.2. Experimental challenges and data analysis limitations

Experimental challenges

The flow rate experiments faced several practical challenges. Air bubbles frequently formed when connecting tubings to the chip or to the needle attached to the syringe, which disrupted the flow rate and caused uneven nutrient supply within the wells. The syringe pump also regularly displayed stalling errors, often due to tubing becoming stuck in the incubator door or due to medium leakage at the tubing–needle connection. In some cases, cells detached from the chip clogged the outlet tubing, which can be explained by the high number of cells found in the exit medium (Table 4.2). These problems were reduced by improving the tubing alignment and flushing the tubings with demineralized water after each experiment.

At some point, a different cell culture medium was used. Although microscopic observation confirmed similar cell morphology and consistent doubling times between the media, small variations in medium composition could have influenced cell viability, nucleus area, or Ki-67 expression. Future experiments should analyze these effects in more detail to determine if different culture media have a significant effect on cells.

Another factor that might have had a significant effect on cell growth and viability is the flow rate. Although ibidi GmbH recommends a flow rate between 0.5 and 1 mL/min [63], this is intended for 3D cell cultures, which are able to tolerate higher shear stress. In this study, however, a 2D monolayer of cells is used, which is more sensitive to a high shear stress. It was therefore chosen to reduce the flow rate to 500 µL/h, after several tests showed cell attachment. During earlier experiments, a flow rate of 400 µL/h was used, since it was part of a plan to test multiple flow rates (400, 800, and 1200 µL/h), but due to time limitations, this was not executed. Moreover, chip-cultured cells exposed to a flow rate were checked throughout the experiments to see whether cells were still attached to the chip or not. Since in some cases cells were washed away (see Table 4.2), a flow rate of 500 µL/h was chosen for further experiments, and higher flow rates were not tested. Nonetheless, testing a broader range, including lower flow rates, could show a more optimal balance between nutrient supply and cell adhesion.

The round geometry of the wells of the chip may also have led to uneven flow dynamics, which could lead to uneven oxygen and nutrient supply throughout the wells. Moreover, chip-cultured cells that were not exposed to a flow rate might have had limited oxygen and nutrient supply, whereas coverslip-cultured cells, which contain more medium volume, were less affected by this, which could have led to higher cell viability.

Another significant challenge was staining the chip-cultured cells. Although ibidi GmbH recommended pipetting the staining solution through the reservoirs, the solution frequently got stuck and failed to pass through the channels to reach the wells. Consequently, the sticky polymer coverslip, which is placed over the wells, was removed carefully and the staining solution was applied directly into the wells. Since the polymer coverslip is flexible and thus easily bends, it had to be removed carefully and temporarily placed on a clean surface during staining. Reattaching the same polymer coverslip may reduce sealing effectiveness compared to its first application. Therefore, replacing it with a new coverslip, such as a glass one, could be considered. However, a glass coverslip might affect microscopy imaging quality if imaging is performed from above, as well as radiation results.

Data analysis limitations

Image segmentation also introduced limitations. The segmentation of Hoechst-stained nuclei was performed using a custom Python code to calculate the cell count and mean nucleus area. While segmentation overall performed well, small inaccuracies were observed, particularly in regions where cells were highly clustered or weakly stained. These inaccuracies may have led to small variations in total cell counts or nuclei areas. Several segmentation results are shown Fig. B.1 in Appendix B.2, where Fig. B.1(c) shows a poorly segmented image due to cell borders not being clearly visible. This occasionally led to overestimated nucleus areas and underestimated cell counts.

Ki-67 image analysis required again cell segmentation in order to detect Ki-67+ cells, which produced slightly different cell counts compared to the same Hoechst-stained images. These differences led to Ki-67+ percentages exceeding 100% if compared to the number of cells segmented from the Hoechst-stained images. Therefore, Ki-67+ fractions were compared to the total number of nuclei detected in each Ki-67 image. Since Ki-67 staining is normally not used for cell counting, segmentation errors affected the result of Ki-67+ counts. An example of under-segmentation is shown in Fig. B.2(c) in Appendix B.4.

Staining with γ-H2AX resulted in poor resolution images where almost no foci were detected, as can be seen in Fig. 4.14(b)-(e). As mentioned in the results, it was therefore chosen to exclude these images for data analysis. The weak γ-H2AX signal could be due to fixating the cells too fast or too late after irradiations to make DSBs visible, poor antibody attachment, or limitations in microscopic imaging. Future work should focus on optimizing the fixation time and using confocal imaging with higher magnifications to possibly improve foci visibility.

Finally, some conditions (e.g. chip exposed to a flow rate and irradiated with 5 Gy protons) had very few microscopic images available for Ki-67 image analysis (see Table 4.6), which limits the reliability of these results. Repeating these experiments with more images could help increase the data's reliability. Moreover, since fixation occurred already 2 hours after irradiation, the image analysis showed early cellular responses, such as morphology changes and proliferation responses. However, long-term responses might also provide interesting outcomes. Including additional time points could help distinguish temporary from long-term radiation responses. Additionally, although both 2 Gy and 5 Gy samples were irradiated, as explained in Chapter 3.4, only the 5 Gy samples were imaged and analyzed due to time limitations.

4.2.3. Recommendations for future research

This section describes several recommendations for future research based on challenges and limitations encountered in this project. The recommendations are categorized by high (immediate changes), medium and low priority (long-term changes).

High priority

Future work should first focus on improving the flow rate conditions inside the chip. As discussed earlier, the applied flow rate of 500 µL/h led to cells being washed away, suggesting that this rate might be too high. Testing a broader range of lower flow rates would help identify a level of shear stress that provides sufficient nutrient supply while cells remain attached.

The formation of air bubbles inside the wells of the chip was another major issue and contributed to additional cell detachment and unevenly flow distribution inside the well. To minimize this, introducing a bubble trap before the entrance of the chip could prevent bubbles from entering the wells. Additionally, bubble formation was observed at tubing connections. Future experiments should therefore find out if using for example Luer-lock fittings or using heat-shrinkage to secure the needle–tubing connections prevents air bubbles from entering the chip.

Finally, data reliability can be improved by obtaining more images per condition. Several conditions in this study were analyzed with a limited number of cells or images, which reduces statistical reliability. At least three images per condition should be collected, ideally from randomly chosen regions of the sample.

Medium priority

Another important area for improvement involves optimization of fixation and staining procedures. Since chip-based fixation was performed by manually pushing the fixation solutions through the inlet of the chip with a syringe, this flow rate may have contributed to more cells being washed away. Developing a more controlled and low-shear fixation method for this microfluidic system would likely reduce this problem and improve reproducibility. Moreover, the recommended staining procedure failed, which calls for a different approach that is achievable and reproducible.

The γ-H2AX staining and analysis also requires optimization, since current images were not useful. Adjusting the fixation time, improving antibody penetration, by testing lower dilutions or testing other antibodies to identify the appropriate one for this cell line, and imaging with confocal microscopy,

potentially including z-stacks, could enhance foci visibility. If γ-H2AX still obtains low foci visibility, other DSBs markers, such as 53BP1, could be additionally used to clarify results.

Expanding the experiment with various time points where cells are fixated after radiation (e.g. 6, 24, and 48 hours, instead of only 2 hours) would perhaps show both early DNA damage and later responses, such as cell-cycle arrest, recovery, proliferation changes or cell death.

Lastly, segmentation and image analysis should be optimized, as segmentation inaccuracies affected the measurement of the nucleus area (overestimation) and cell counts (underestimation). Improving various parameters such as the threshold or segmentation method might increase segmentation accuracy.

Low priority

Several more long-term changes could further enhance the relevance and accuracy of the model. One factor is the surface coating of the wells of the chip. The chips that were used in this study were pre-coated with ibiTreat, which makes the surface hydrophilic and adhesive. However, testing other coatings, such as gelatin or fibronectin, or using uncoated chips as controls, may help understand and improve the adhesion of FaDu cells under flow rate conditions.

It may also be helpful to perform control experiments comparing different cell culture media, as media composition can influence proliferation and morphology. Making sure that the type of medium does not add experimental variability is important for experimental reproducibility.

Future studies could also combine FaDu cells with other cell types, such as fibroblasts, macrophages, or T cells, to study how flow rate and radiation affect for example tumor–immune interactions.

Finally, switching from 2D monolayers to 3D models, such as spheroids, organoids, or patient-derived tumor tissue, would better mimic the tumor microenvironment which could give more insights into *in vivo* representative tumor responses in radiobiology experiments.

5

Conclusion

This thesis investigated the influence of flow rate and radiation type (X-ray and proton) on FaDu cell behavior in a microfluidic chip system compared to conventional coverslip cultures. Using assays for cell adhesion, morphology and proliferation, the study demonstrated that the chip environment, both with and without a flow rate, induces measurable differences in cellular responses after irradiation.

Although a flow rate of 500 µL/h led to cell detachment, the cells that remained showed higher proliferation activity and larger nuclei than coverslip cultures. This suggests that applied mechanical forces and the chip environment influence cell physiology in ways that could be relevant for radiobiological studies. Data obtained from the exit medium shows that dead cells were consistently larger than live cells, and that both live and dead cells increased in size after irradiation. This pattern may indicate that many of the detached, non-viable cells were in the G2/M phase, which is characterized by larger nuclei and increased radiosensitivity. As a result, the remaining adherent cells may include smaller, more resilient cells, altering the morphology and proliferation results.

In addition, the comparison between X-ray- and proton–irradiated samples indicated that the two radiation modalities induce early effects on cell morphology, which may reflect subtle differences in cell-cycle phase distribution or DNA damage response. These results show how measuring the nucleus area can provide insight into the cell's physiological state after irradiation.

Despite experimental challenges, such as air bubble formation, limited image numbers and image segmentation inaccuracies, the study successfully set up and tested an experimental workflow that combined cells cultured on a microfluidic chip, radiation exposure and automated image analysis. The results show that these on-a-chip systems have strong potential for studying radiation responses under more physiologically relevant conditions than standard static cultures.

Based on the insights obtained from the results, there are several recommendations for future research. Optimizing the flow rate conditions, improving fixation and staining protocols and increasing the number of images per condition will significantly enhance data reliability and reproducibility. Testing various DNA damage assays, including longer time points in which the cells are fixated after irradiation and better image analysis techniques could further deepen the biological interpretation of the results. In the longer term, testing other surface coatings, including co-cultures of different cell types, or use 3D tumor models would make the platform more representative of the *in vivo* tumor microenvironment and increases its application in the field of radiobiology.

Overall, this thesis provides a successful proof-of-principle experimental setup for future microfluidic radiation studies. While more optimization is needed, the work shows both the feasibility and the potential advantages of cells cultured in on-a-chip system for understanding how tumor cells respond to different radiation conditions and mechanical environments. With technical improvements and biological refinement, this on-a-chip setup could become a powerful tool for preclinical radiotherapy research.

References

[1] Xiaomei Ma and Herbert Yu. "Global burden of cancer". In: *The Yale journal of biology and medicine* 79.3-4 (2007), p. 85.

[2] Yuxi Liu and Zhibo Zheng. "Understanding the global cancer statistics 2022: growing cancer burden". In: *Science China Life Sciences* 67.10 (2024), pp. 2274–2276.

[3] Tim Heemskerk et al. "Position in proton Bragg curve influences DNA damage complexity and survival in head and neck cancer cells". In: *Clinical and Translational Radiation Oncology* 51 (2025), p. 100908.

[4] M Lupu-Plesu et al. "Effects of proton versus photon irradiation on (lymph) angiogenic, inflammatory, proliferative and anti-tumor immune responses in head and neck squamous cell carcinoma". In: *Oncogenesis* 6.7 (2017), e354–e354.

[5] Tai-Ze Yuan, Ze-Jiang Zhan, and Chao-Nan Qian. "New frontiers in proton therapy: applications in cancers". In: *Cancer Communications* 39.1 (2019), p. 61.

[6] Jerome Lacombe, Shanna Leslie Phillips, and Frederic Zenhausern. "Microfluidics as a new tool in radiation biology". In: *Cancer letters* 371.2 (2016), pp. 292–300.

[7] Peter W Nagle and Robert P Coppes. "Current and future perspectives of the use of organoids in radiobiology". In: *Cells* 9.12 (2020), p. 2649.

[8] Saskia Hazout et al. "Historical view of the effects of radiation on cancer cells". In: *Oncology Reviews* 19 (2025), p. 1527742.

[9] Reem Ahmad et al. "Particle beam radiobiology status and challenges: a PTCOG radiobiology subcommittee report". In: *International Journal of Particle Therapy* 13 (2024), p. 100626.

[10] Rohollah Nasiri, Arnav Sankaranthi, and Guillem Pratx. "Organ-on-a-chip systems for modeling tumor and normal tissue microenvironments in radiotherapy research". In: *Trends in Biotechnology* (2025).

[11] Dongeun Huh et al. "Reconstituting organ-level lung functions on a chip". In: *Science* 328.5986 (2010), pp. 1662–1668.

[12] Sangeeta N Bhatia and Donald E Ingber. "Microfluidic organs-on-chips". In: *Nature biotechnology* 32.8 (2014), pp. 760–772.

[13] Yi Quan et al. "Organ-on-a-chip: The next generation platform for risk assessment of radiobiology". In: *RSC advances* 10.65 (2020), pp. 39521–39530.

[14] Daniel E Johnson et al. "Head and neck squamous cell carcinoma". In: *Nature reviews Disease primers* 6.1 (2020), p. 92.

[15] Julia Ostapowicz et al. "Improving therapeutic strategies for Head and Neck Cancer: Insights from 3D hypoxic cell culture models in treatment response evaluation". In: *Advances in Medical Sciences* 69.2 (2024), pp. 368–376.

[16] Davide Perico and Pierluigi Mauri. "Deciphering Radiotherapy Resistance: A Proteomic Perspective". In: *Proteomes* 13.2 (2025), p. 25.

[17] Chia-Lun Chang et al. "Comparing the oncologic outcomes of proton therapy and intensity-modulated radiation therapy for head and neck squamous cell carcinoma". In: *Radiotherapy and Oncology* 190 (2024), p. 109971.

[18] Laura Vanderwaeren et al. "Clinical progress in proton radiotherapy: biological unknowns". In: *Cancers* 13.4 (2021), p. 604.

[19] SL Gulliford and KM Prise. "Relative biological effect/linear energy transfer in proton beam therapy: a primer". In: *Clinical Oncology* (2019).

[20] International Atomic Energy Agency. *Radiation Oncology Physics: A Handbook for Teachers and Students*. Available from the International Atomic Energy Agency. Vienna: IAEA, 2005. URL: https://www-pub.iaea.org/MTCD/Publications/PDF/Pub1196_web.pdf.

[21] Rodin Chermat et al. "Radiotherapy on-chip: microfluidics for translational radiation oncology". In: *Lab on a Chip* 22.11 (2022), pp. 2065–2079.

[22] John D Cramer et al. "The changing therapeutic landscape of head and neck cancer". In: *Nature reviews Clinical oncology* 16.11 (2019), pp. 669–683.

[23] Emil H Grubbé. "Priority in the therapeutic use of X-rays". In: *Radiology* 21.2 (1933), pp. 156–162.

[24] David S Chang et al. *Basic radiotherapy physics and biology*. Tech. rep. Springer, 2014.

[25] Radhe Mohan. "A review of proton therapy–Current status and future directions". In: *Precision radiation oncology* 6.2 (2022), pp. 164–176.

[26] Wayne D Newhauser and Rui Zhang. "The physics of proton therapy". In: *Physics in Medicine & Biology* 60.8 (2015), R155.

[27] Qais Akolawala and Angelo Accardo. "Engineered Cell Microenvironments: A Benchmark Tool for Radiobiology". In: *ACS Applied Materials & Interfaces* 17.4 (2025), pp. 5563–5577.

[28] Eloïse Bouges et al. "Human intestinal organoids and microphysiological systems for modeling radiotoxicity and assessing radioprotective agents". In: *Cancers* 15.24 (2023), p. 5859.

[29] Martine E Lomax, Lisa K Folkes, and Peter O'Neill. "Biological consequences of radiation-induced DNA damage: relevance to radiotherapy". In: *Clinical oncology* 25.10 (2013), pp. 578–585.

[30] G. Hubinger et al. *Doubling time of FaDu cells*. https://bio-protocol.org/exchange/minidetail?id=18159313&type=30. Accessed: 2025-11-09. 2022.

[31] Ebony Potts. *G0 Phase of the Cell Cycle | Overview & Importance*. https://study.com/skill/practice/analyzing-the-role-of-the-g0-phase-in-the-cell-cycle-questions.html. Accessed: 2025-11-10. 2023.

[32] Kristina Claesson et al. "RBE of α-particles from 211At for complex DNA damage and cell survival in relation to cell cycle position". In: *International journal of radiation biology* 87.4 (2011), pp. 372–384.

[33] Lucie A Low and Danilo A Tagle. "Tissue chips to aid drug development and modeling for rare diseases". In: *Expert opinion on orphan drugs* 4.11 (2016), pp. 1113–1121.

[34] Neda Azizipour et al. "Evolution of biochip technology: A review from lab-on-a-chip to organ-on-a-chip". In: *Micromachines* 11.6 (2020), p. 599.

[35] Chak Ming Leung et al. "A guide to the organ-on-a-chip". In: *Nature Reviews Methods Primers* 2.1 (2022), p. 33.

[36] Yisha Huang et al. "From organ-on-a-chip to human-on-a-chip: A review of research progress and latest applications". In: *ACS sensors* 9.7 (2024), pp. 3466–3488.

[37] Jiasheng Yan et al. "Organ-on-a-chip: A new tool for in vitro research". In: *Biosensors and Bioelectronics* 216 (2022), p. 114626.

[38] Yanjun Liu, Ling Lin, and Liang Qiao. "Recent developments in organ-on-a-chip technology for cardiovascular disease research". In: *Analytical and Bioanalytical Chemistry* 415.18 (2023), pp. 3911–3925.

[39] Donald E Ingber. "Human organs-on-chips for disease modelling, drug development and personalized medicine". In: *Nature Reviews Genetics* 23.8 (2022), pp. 467–491.

[40] Negar Farhang Doost and Soumya K Srivastava. "A comprehensive review of organ-on-a-chip technology and its applications". In: *Biosensors* 14.5 (2024), p. 225.

[41] R Nithin et al. "Organ-on-a-chip: an emerging research platform". In: *Organogenesis* 19.1 (2023), p. 2278236.

[42] Jihoon Ko et al. "Engineering organ-on-a-chip to accelerate translational research". In: *Micromachines* 13.8 (2022), p. 1200.

[43] Jing Kong et al. “A novel microfluidic model can mimic organ-specific metastasis of circulating tumor cells”. In: *Oncotarget* 7.48 (2016), p. 78421.

[44] ibidi GmbH. *Cell Culture Under Flow: Application Guide*. `https://ibidi.com/img/cms/downloads/FL_AG_034_Cell_Culture_Under_Flow_150dpi.pdf`. Accessed: 2025-11-13. 2020.

[45] Stephanie Lehoux. “Molecular mechanisms of the vascular responses to hemodynamic forces”. In: *Biomechanics of coronary atherosclerotic plaque* (2021), pp. 49–83.

[46] CE Staicu et al. “Glass lab-on-a-chip platform fabricated by picosecond laser for testing tumor cells exposed to X-ray radiation”. In: *Applied Physics A* 128.9 (2022), p. 770.

[47] Simon D Carr et al. “Analysis of radiation-induced cell death in head and neck squamous cell carcinoma and rat liver maintained in microfluidic devices”. In: *Otolaryngology–Head and Neck Surgery* 150.1 (2014), pp. 73–80.

[48] Ramsah Cheah et al. “Measuring the response of human head and neck squamous cell carcinoma to irradiation in a microfluidic model allowing customized therapy”. In: *International journal of oncology* 51.4 (2017), pp. 1227–1238.

[49] Bishnubrata Patra et al. “On-chip combined radiotherapy and chemotherapy testing on soft-tissue sarcoma spheroids to study cell death using flow cytometry and clonogenic assay”. In: *Scientific reports* 9.1 (2019), p. 2214.

[50] Maeva Bavoux et al. “X-ray on chip: Quantifying therapeutic synergies between radiotherapy and anticancer drugs using soft tissue sarcoma tumor spheroids”. In: *Radiotherapy and Oncology* 157 (2021), pp. 175–181.

[51] Sagar Regmi et al. “Applications of microfluidics and organ-on-a-chip in cancer research”. In: *Biosensors* 12.7 (2022), p. 459.

[52] Lucie A Low et al. “Organs-on-chips: into the next decade”. In: *Nature Reviews Drug Discovery* 20.5 (2021), pp. 345–361.

[53] Raquel Alonso-Roman et al. “Organ-on-chip models for infectious disease research”. In: *Nature microbiology* 9.4 (2024), pp. 891–904.

[54] E Markova, N Schultz, and IY Belyaev. “Kinetics and dose-response of residual 53BP1/γ-H2AX foci: Co-localization, relationship with DSB repair and clonogenic survival”. In: *International journal of radiation biology* 83.5 (2007), pp. 319–329.

[55] Kai Rothkamm et al. “Pathways of DNA double-strand break repair during the mammalian cell cycle”. In: *Molecular and cellular biology* 23.16 (2003), pp. 5706–5715.

[56] Thomas Scholzen and Johannes Gerdes. “The Ki-67 protein: from the known and the unknown”. In: *Journal of cellular physiology* 182.3 (2000), pp. 311–322.

[57] E Wulf et al. “Fluorescent phallotoxin, a tool for the visualization of cellular actin.” In: *Proceedings of the national academy of sciences* 76.9 (1979), pp. 4498–4502.

[58] Inc. Biotium. *Hoechst 33258, Product and Safety Data Sheet (Cat. No. 40044, 40045)*. `https://biotium.com/wp-content/uploads/2016/12/PI-40044-40045.pdf`. Accessed: 2025-11-11. 2019.

[59] Molecular Expressions Florida State University and the Microscopy & Imaging Facility. *Overview of Excitation and Emission Fundamentals*. `https://micro.magnet.fsu.edu/primer/lightandcolor/fluoroexcitation.html`. Accessed: 2025-11-11. 2018.

[60] M Rovituso et al. “Characterisation of the HollandPTC R&D proton beamline for physics and radiobiology studies”. In: *Physica Medica* 130 (2025), p. 104883.

[61] Tim Heemskerk et al. “Enhanced radiosensitivity of head and neck cancer cells to proton therapy via hyperthermia-induced homologous recombination deficiency”. In: *Clinical and Translational Radiation Oncology* 51 (2025), p. 100898.

[62] Giuseppe La Verde et al. “Cytoskeleton response to ionizing radiation: a brief review on adhesion and migration effects”. In: *Biomedicines* 9.9 (2021), p. 1102.

[63] ibidi GmbH. *Instructions µ-Slide III 3D Perfusion*. Instruction Manual. `https://ibidi.com/channel-slides/53--slide-iii-3d-perfusion.html`. ibidi GmbH. 2021.

A

Protocols

A.1. Cell Preparation

A.1.1. Cell Passage

Table A.1 gives an overview of all the required equipment and materials for cell passage. Afterwards, a step-by-step protocol for cell passage is given.

Table A.1: Required equipment and materials for cell passage

Item	**Quantity**	**Notes**
Cell culture medium	15 to 25 mL	Pre-warmed to 37°C. Volume depending on flask quantity and size
PBS buffer	1 to 3 mL	Pre-warmed to 37°C. Volume depending on flask quantity and size
Water bath (37°C)	1	For warming medium and PBS
Fume hood	1	For sterile working environment
Ethanol (disinfectant)	Several mL	For cleaning and sterilization
Plastic bag	1	For tripod waste bin
Tripod	1	For waste collection
Pipettes and tips	Multiple	Disposable; used for medium, PBS, trypsin, and cell suspension
Sterile tubes	1	For collecting and diluting cell suspension
Cell culture flasks	1 or 2	Labeled with cell type, dilution, name, and date; 25 or 75 cm^2
Permanent marker	1	For labeling flasks
Gas source	1	For sterilization
Suction tool	1	For removing liquids from flasks
Microscope	1	For checking flasks
Trypsin	500 µL to 1 mL	At 4°C. Volume depending on flask type
Incubator (37°C, 5% CO_2)	1	For cell culture flask incubation

1. Add 4.5 to 10 mL (depending on the amount and size of the culture flask) of cell culture medium into each new flask. Label them with cell type, dilution, name and date
2. Observe the cells from the incubated flask under a microscope. Floating cells may indicate cell death due to overgrowth. This means the flask is full and cells are ready to be passaged
3. Sterilize the suction tool by briefly holding it above the gas
4. Remove the old medium using the suction tool while inverting the flask (cells adhere to the bottom)

5. Sterilize and store the suction tool
6. Invert the flask again and rinse with PBS (1 to 3 mL, depending on the size of the flask)
7. Remove PBS again using the suction tool
8. Add 500 µL to 1 mL (depending on the size of the culture flask) of trypsin into the flask
9. Incubate flask for 5 minutes.
10. Check for cell detachment under the microscope
11. Add 1.5 or 3 mL of medium into the flask. Pipette up and down to mix the cells homogeneously
12. Transfer the mixture (2 or 4 mL total) to a tube
13. Transfer the mixture into the new flasks. The volume depends on the desired dilution. Pipette multiple times for homogeneity
14. Gently shake the flasks (side-to-side, top-to-bottom) to distribute cells evenly and place them inside the incubator

A.1.2. Cell Seeding

Table A.2 gives an overview of the required equipment and materials for cell seeding. Afterwards, a step-by-step protocol is given.

Table A.2: Required equipment and materials for cell seeding

Item	**Quantity**	**Notes**
Cell suspension	4 mL	Collected after Cell Passage Protocol step 12
Viability dye	20 µL	
Pipettes and tip	Multiple	For transferring cell mixture, medium and PBS
Countess slide	1	Used in automated cell counter
Countess 3 Automated Cell Counter	1	For measuring concentration and viability
18 mm glass coverslips	1 per well	Placed in 12-well plate wells
12-well plate	1	For coverslip seeding; unused wells filled with PBS
Cell culture medium	Several mL	1 mL per well in 12-well plate; 50µL per chip reservoir
PBS	Several mL	Used to prevent evaporation and for humidification
Ibidi chip	1	For cell seeding
Petri dish	1	For holding and humidifying ibidi chip
Tissue (moistened)	1	Placed in petri dish with 3 mL PBS
Incubator (37°C, 5% CO_2)	1	For incubating both the 12-well plate (48 hours) and chip (24 hours)

Note: Follow the Cell Passage Protocol (Section A.1.1) until step 12 is completed and the cell mixture is collected. Then:

1. Mix 20 µL of the cell suspension with 20 µL of the viability dye
2. Pipette the 40 µL mixture into a Countess slide (see Fig 3.4a) and insert it into the Countess 3 Automated Cell Counter to determine:
   - Cell concentration (cells/mL)
   - Percentage of live and dead cells
3. Use the Countess 3 dilution calculator to dilute the cell suspension to approximately 1.0×10^5 cells/mL

4. Place an 18 mm glass coverslip into each well in the 12-well plate and pipette 150 µL of the diluted mixture and 1 mL of cell culture medium on top of it
5. Fill all unused wells in the 12-well plate with 1 mL of PBS to prevent evaporation during incubation
6. Close the plate with its lid and place it in a 37°C, 5% CO_2 incubator for 48 hours
7. Pipette 30 µL of the diluted mixture into each well of the ibidi chip
8. Add 50 µL of medium to each reservoir of the ibidi chip to prevent drying out
9. Place the chip in a petri dish containing a tissue moistened with approximately 3 mL of PBS
10. Cover the chip with its lid and incubate at 37°C, 5% CO_2 for 24 hours

A.1.3. Cell Fixation

Table A.3 gives an overview of the required equipment and materials for cell fixation. Afterwards, a step-by-step protocol is given.

Table A.3: Required equipment and materials for cell fixation

Item	**Quantity**	**Notes**
PBS	15 mL	For washing and flushing
PFA mixture	10 mL	For 50 mL 4% PFA mixture: mix 5 mL 37% PFA with 45 mL PBS
Parafilm	A few cm	To seal chip reservoirs before storage
10 mL syringes	2	One for PBS, one for PFA mixture
Pipettes and tips	Several	Used for fixating cells on coverslips in 12-well plate
Waste container	1	For collecting fluids during chip flushing
Refrigerator (7°C)	1	For storing fixed samples

For the 12-well plate, cell fixation is done as follows:

1. Remove the cell culture medium from the wells of the 12-well plate. Be careful not to scratch the coverslip as cells are attached to it. **Note:** Total volumes inside the wells: 30 µL for each ibidi well, 50 µL for each reservoir, and 1150 µL for each 12-well plate well
2. Wash each well that contains cells with 1 mL PBS
3. Add 1 mL of the PFA mixture into the wells and incubate for 5 minutes at room temperature
4. Remove the PFA mixture from the wells
5. Add 1 mL PBS to each well and store the plate in the refrigerator at 4°C

For the ibidi chip, the cell fixation steps are slightly different due to the wells being covered with the polymer coverslip. Therefore, instead of pipetting the fluids in and out, a syringe is used instead:

1. Disconnect the tubing from the reservoirs
2. Fill two 10 mL syringes: one with 6 mL of PBS (pre-warmed to 37°C and another with 3 mL of the PFA mixture (at 4°C)
3. Place the syringe containing PBS on the inlet reservoir and slowly push 1 mL through the channels. Place a cup underneath the chip and hold the chip slightly tilted so the fluids coming out are collected in the cup. Repeat for every inlet reservoir and make sure the cell culture medium is completely gone
4. Repeat this process using the PFA mixture and incubate for 5 minutes and room temperature
5. Finally, flush again with PBS. Make sure the reservoirs are filled with PBS as well. Seal the reservoir with a piece of Parafilm and store the chip in the refrigerator at 4°C

A.2. Manual for Setting Up Flow Rate Experiments

Table A.4 gives an overview of the required equipment and materials for setting up the flow rate experiments. Afterwards, a step-by-step protocol is given.

Table A.4: Required equipment and materials for setting up flow rate experiments

Item	**Quantity**	**Notes**
Cell mixtures	20 & 180 µL	Diluted to $0.7-1.7 \times 10^5$ cells/mL
Parafilm	2 small piece	Used for mixing cells and viability dye and to prevent leakage at needle–tube interface
Viability dye	20 µL	Mixed with cell mixture (20 µL) for cell counting
Countess slide	1	For automated cell counting
Countess 3 Automated Cell Counter	1	Used to determine cell concentration
Cell culture medium	15 mL	For dilution, reservoirs and filling tubings
Pipettes and tip	Multiple	For transferring cell mixture, medium and PBS
Ibidi chip	1	Used for cell seeding and perfusion
Sterile petri dish	1	Used to hold chip during incubation
Tissue	1 piece	Moistened with PBS
Sterile PBS	3–4 mL	Used to moisten tissue in petri dish
Syringe pump	1	Flow rate: 500 µL/h; continuous pumping
10 mL syringe	1	Diameter 15.0 mm
Needle	1	Attached to syringe, used for tubing connection
Coverslip	1	Seals the ibidi chip
Tweezers	1	Used to place coverslip over the wells
Luer connectors	2	For tubing-chip connections
Tubings	2	Connect syringe and chip
Cup	1	Collects outlet medium, secured with tape
Tape	Small piece	Used to secure the outlet tubing to the cup
Demi water	1 syringe volume	Used for flushing tubings

Note: Follow the Cell Passage Protocol (Section A.1.1) until step 12 is completed and the cell mixture is collected. Then:

1. Take 20 µL of the cell mixture and place it on a closed piece of Parafilm. Add 20 µL of the viability dye and pipette up and down several times to ensure homogeneity. Take 20 µL of the resulting mixture of cells and viability dye and pipette it into the Countess slide. Insert it into the Countess 3 Automated Cell Counter to measure the number of cells/mL. Ibidi recommends a cell concentration of approximately $0.7-1.7 \times 10^5$ cells/mL. Dilute the cell mixture in a new tube to a concentration within this range using cell culture medium. Use this diluted cell mixture for the ibidi chip
2. Add 30 µL of this cell mixture into each well and fill the reservoirs completely with cell culture medium. Cover the slide with the lid. Put a piece of tissue in a sterile petri dish and add approximately 3–4 mL of sterile PBS to moisten the tissue. Place the chip inside the dish on top of the tissue, place the dish inside the incubator and wait for cell attachment (around 1 day)
3. After one day, refill the wells and reservoirs with cell culture medium, as they might be dried out
4. Prepare the syringe pump: specify the syringe diameter (15.0 mm for a 10 mL syringe), set the flow rate (select the correct unit, µL/h, and flow rate, 500). Ensure the pump is set to 'pumping' and not 'withdrawing'. Set the volume to zero so that it pumps continuously until manually stopped

5. Fill the syringe with 10 mL cell culture medium and mount it in the holder of the pump. Attach a needle to the syringe.

Note: Ensure that the gray cylindrical component (the pusher block) is positioned completely to the right (towards the syringe) to prevent pumping failure.

6. Remove the white strip from the chip and place the coverslip on top with tweezers. Press gently with a finger to ensure a tight seal
7. Attach the tubes to the Luer connectors. Attach the left tube to the needle, but be careful since the needle can easily puncture the tubing. Cover this connection with a piece of Parafilm to prevent leakage and test for leakage by gently pushing the syringe. Place the right tube into a cup and secure it with a piece of tape
8. Fill the tubes completely with cell culture medium. Then, attach both connectors to the left and right reservoir of the chip
9. Place the chip and tubings inside the incubator and start the syringe pump (located outside the incubator) for 20 hours
10. After 20 hours, perform the radiation experiment (Section 3.4)
11. Meanwhile, flush the tubings first with air to remove all medium, and connect the tubes to a clean chip (no cells or medium, sealed with a coverslip). Fill a syringe with demineralized water (with needle attached) and place it in the syringe pump. Connect the inlet tube to the syringe. Use a high flow rate (e.g., 2 mL/h) to flush the tubings and prevent it from clogging
12. Repeat steps 4 to 9 for the second application of flow rate for 2 hours

A.3. Immunocytochemistry Fluorescence

Table A.5 gives an overview of the required equipment and materials for staining the coverslips of the 12-well plate and the ibidi chip. Afterwards, a step-by-step protocol is given. The staining protocol has been provided by LUMC and adapted for the 12-well plate and the ibidi chip.

Table A.5: Required equipment and materials for immunostaining

Item	Quantity	Notes
PBS	Variable (0.5 mL for 12-well plate wells, 30 µL for wells ibidi chip)	Used for washing
0.2% Triton X-100 (source) in PBS	See quantity PBS	For cell permeabilization
5% BSA (source) in PBS	See quantity PBS	Blocking solution to prevent non-specific binding
1% BSA in PBS	For antibody dilutions	Used for diluting primary and secondary antibodies
Primary antibodies (γ-H2AX, Ki-67)	30 µL drops on Parafilm for coverslip and 30 µL for the chip	Incubated overnight in humid chamber at 4°C
Secondary antibodies (Alexa 488, Alexa 647)	1:500 dilution	Incubated for 1 hour at room temperature
Phalloidin-TRITC	1:200 to 1:500 dilution	For cytoskeleton staining
Hoechst 33258	1:1000 dilution	Incubated 5 minutes at room temperature
Vectashield mounting medium	20 µL drop	Used for mounting coverslips on glass slides
Parafilm	As needed	For antibody incubation for coverslips
Tweezers	1 pair	For moving coverslips
Glass slides	1 per 2 coverslips	For final mounting coverslips
Ethanol	A few mL	For cleaning glass slides
Aluminum foil	As needed	For light protection during and after staining
Dark storage box	1	Storage of mounted samples overnight
Humid chamber	1	For antibody incubations
Pipettes and tip	Multiple	For transferring PBS, BSA and antibodies

12-well plate

Day 1: Primary antibodies

1. Remove PBS from the wells
2. Add 0.5 mL 0.2% Triton X-100 in PBS in each well and incubate for 15 minutes at room temperature (to permeabilize cells for intracellular staining)
3. Remove the Triton X-100 and wash once with 0.5 mL PBS
4. Add 0.5 mL 5% BSA in PBS and incubate for 30 minutes to 1 hour in a humid chamber at room temperature (to block non-specific binding sites)
5. Cut a piece of Parafilm and label it with the radiation dose (Gy), type, and antibodies used. Add 30 µL drops of primary antibody solution onto the Parafilm. Using tweezers, place each coverslip from the well upside down onto a drop
6. Incubate with primary antibodies (γ-H2AX, Ki-67) in 1% BSA/PBS in a humid chamber overnight at 4°C

Day 2: Secondary antibodies

7. Remove the BSA from the wells and add 0.5 mL PBS
8. Place the coverslips upside down back into the wells with the tweezers and wash 2 times with PBS
9. Repeat blocking step (Step 4) using secondary antibody solution
10. Incubate with conjugate (Phalloidin-TRITC) and secondary antibodies (Alexa 488 and Alexa 647) in 1% BSA/PBS for 1 hour at room temperature in the dark humid chamber. Use appropriate individual dilutions
11. Return the coverslips to the 12-well plate
12. Wash 2 times with 0.5 mL PBS, 5 minutes each
13. Counterstain with Hoechst 33258 (1:1000) for 5 minutes
14. Wash once with 0.5 mL PBS
15. Clean a glass slide with ethanol
16. Label the slide with radiation type, dose (Gy), staining date and cell type
17. Place two drops (20 µL each) of Vectashield mounting medium on the slide
18. Use tweezers to place the stained coverslip upside down onto the drops
19. Store the slide in a dark box at room temperature for 1 day. Afterwards, wrap it in aluminum foil and store it in the refrigerator (4°C)

ibidi chip

Day 1: Primary antibodies

1. Remove the polymer coverslip from the ibidi slide and place the sticky side on top of a clean piece of aluminum foil
2. Remove PBS from the wells and reservoirs
3. Add 30 µL 0.2% Triton X-100 in PBS in each well and incubate for 15 minutes at room temperature (to permeabilize cells for intracellular staining)
4. Remove Triton X-100 and wash once with 30 µL PBS
5. Add 30 µL 5% BSA in PBS in each well and incubate for 30 minutes to 1 hour in a humid chamber at room temperature (to block non-specific binding sites)
6. Remove the 5% BSA in PBS and incubate with 30 µL of the primary antibodies (γ-H2AX, Ki-67) in 1% BSA/PBS in a humid chamber overnight at 4°C

Day 2: Secondary antibodies

7. Remove the primary antibodies
8. Repeat blocking step (Step 5) using secondary antibody solution
9. Incubate with conjugate (Phalloidin-TRITC) and secondary antibodies (Alexa 488 and Alexa 647) in 1% BSA/PBS for 1 hour at room temperature in a dark humid chamber
10. Wash 2 times with 30 µL PBS, 5 minutes each
11. Counterstain with 30 µL Hoechst 33258 (1:1000) for 5 minutes
12. Wash once with 30 µL PBS
13. Put the polymer coverslip back on the chip on top of the wells. Press down with a finger to make sure it is tightly sealed. Wrap the chip in aluminum foil and store it in the refrigerator (4°C)

B

Image analysis

B.1. Python Code for Hoechst 33258 Image Analysis

Listing B.1: Python script for automated Hoechst 33825 nuclei segmentation and quantification of multiple images

```python
# Hoechst Image Analysis - Multiple Screenshot Images

from pathlib import Path
import cv2
import numpy as np
import pandas as pd
import matplotlib.pyplot as plt
from skimage import filters, morphology, segmentation, feature, measure
from scipy import ndimage as ndi

folder_path = Path(r"path_to_folder")    # Folder with images
scale_bar_um = 50          # Scale bar length in µm
scale_bar_px = 56          # Scale bar length in pixels (measured in ImageJ)
min_area_um2 = 75          # Exclude objects smaller than this (µm²)
max_area_um2 = 1500        # Exclude objects larger than this (µm²)
watershed_min_distance_um = 15.0  # Expected minimal separation between nuclei centers (µm)

# Pixel size and area
px_x_um = px_y_um = float(scale_bar_um) / float(scale_bar_px)
pixel_area_um2 = px_x_um * px_y_um
print(f"Pixel size = {px_x_um:.4f} µm/px → Pixel area = {pixel_area_um2:.4f} µm²")

# Gather images
image_paths = list(folder_path.glob("*.png")) + list(folder_path.glob("*.jpg"))
print(f"Found {len(image_paths)} images to process.")

summary_rows = []

# PROCESS EACH IMAGE
for image_path in image_paths:
    print(f"\nProcessing: {image_path.name}")

    # Load image and extract Hoechst channel (blue)
    im_bgr = cv2.imread(str(image_path))
    if im_bgr is None:
        print(f"Could not open image: {image_path}")
        continue

    hoechst_img = im_bgr[:, :, 0]  # Blue channel in BGR order

    # Normalize to uint8
    img = hoechst_img.copy()
    if img.dtype != np.uint8:
        img = (255 * (img - img.min()) / (img.max() - img.min())).astype(np.uint8)
```

```
45
46      # Denoise + threshold
47      blur = cv2.GaussianBlur(img, (3, 3), 0)
48      th = filters.threshold_otsu(blur)
49      binary = blur > th
50
51      # Remove small objects and close holes
52      min_area_px = max(1, int(np.round(min_area_um2 / pixel_area_um2)))
53      binary = morphology.remove_small_objects(binary, min_size=min_area_px)
54      binary = morphology.binary_closing(binary, morphology.disk(2))
55
56      # Distance transform + watershed
57      distance = ndi.distance_transform_edt(binary)
58      min_dist_px = max(3, int(round(watershed_min_distance_um / px_x_um)))
59      local_max = feature.peak_local_max(distance,
60                                         indices=False,
61                                         footprint=np.ones((min_dist_px, min_dist_px)),
62                                         labels=binary)
63      markers = ndi.label(local_max)[0]
64      labels_ws = segmentation.watershed(-distance, markers, mask=binary)
65
66      # Measure nuclei
67      props = measure.regionprops(labels_ws)
68      areas_um2 = np.array([p.area * pixel_area_um2 for p in props])
69      diameters_um = 2.0 * np.sqrt(areas_um2 / np.pi)
70
71      # Build DataFrame
72      rows = []
73      for i, p in enumerate(props):
74          rows.append({
75              "label": i + 1,
76              "area_um2": areas_um2[i],
77              "equiv_diameter_um": diameters_um[i],
78              "centroid_y": p.centroid[0],
79              "centroid_x": p.centroid[1]
80          })
81      df = pd.DataFrame(rows)
82
83      # Filter by area
84      df_filtered = df[(df["area_um2"] >= min_area_um2) & (df["area_um2"] <= max_area_um2)].
            copy()
85      df_filtered = df_filtered.sort_values("area_um2", ascending=False).reset_index(drop=True)
86
87      # VISUALIZATION: Overlay boundaries + labels
88
89      plt.figure(figsize=(8, 8))
90      plt.imshow(hoechst_img, cmap="gray")
91      bound = segmentation.mark_boundaries(np.stack([hoechst_img]*3, axis=-1)/255.0, labels_ws,
            color=(1, 0, 0))
92      plt.imshow(bound, alpha=0.6)
93
94      # Label all detected nuclei
95      for i, row in df_filtered.iterrows():
96          y, x = row["centroid_y"], row["centroid_x"]
97          plt.text(x, y, str(i + 1), color="yellow", fontsize=6, ha="center", va="center")
98
99      plt.title(f"{image_path.name} - {len(df_filtered)} nuclei")
100     plt.axis("off")
101
102     # Save overlay
103     overlay_path = folder_path / f"{image_path.stem}_overlay.png"
104     plt.savefig(overlay_path, dpi=150, bbox_inches="tight")
105     plt.close()
106     print(f"Saved overlay image to {overlay_path}")
107
108     # Save per-nucleus CSV
109     out_csv = folder_path / f"{image_path.stem}_nuclei_areas.csv"
110     df_filtered.to_csv(out_csv, index=False)
111     print(f"Saved per-nucleus CSV to {out_csv}")
112
113     # Summary stats
```

```
    if len(df_filtered) > 0:
        total_cells = len(df_filtered)
        min_area = df_filtered["area_um2"].min()
        max_area = df_filtered["area_um2"].max()
        mean_area = df_filtered["area_um2"].mean()
    else:
        total_cells = 0
        min_area = max_area = mean_area = 0.0

    summary_rows.append({
        "image_name": image_path.name,
        "total_cells": total_cells,
        "min_area_um2": round(min_area, 1),
        "max_area_um2": round(max_area, 1),
        "mean_area_um2": round(mean_area, 1)
    })

# SUMMARY ACROSS ALL IMAGES

summary_df = pd.DataFrame(summary_rows)
summary_csv = folder_path / "nuclei_summary_per_image.csv"
summary_df.to_csv(summary_csv, index=False)

print("\nSummary saved to:", summary_csv)
print(summary_df)
```

B.2. Results from Hoechst 33258 Image Analysis

Fig. B.1 shows example Hoechst-stained images with segmentation overlays generated by the custom Python code. The overlays illustrate the code's ability to segment and identify individual nuclei (a) and (d), as well as its limitations in densely packed or overlapping regions (b) and (c). These examples were included to show the variability in segmentation accuracy, which may have influenced image analysis outcomes.

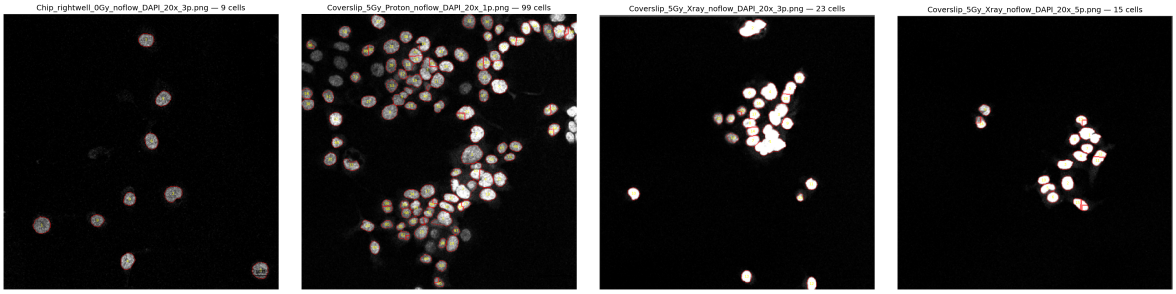

(a) **(b)** **(c)** **(d)**

Figure B.1: Several Hoechst segmentation overlay images produced after processing Hoechst-stained images with a custom Python code. (a) shows the result of image processing static non-irradiated chip-cultured cells, imaged with a magnification of 20×. (b), (c) and (d) show the results of image processing coverslip-cultured cells exposed to 5 Gy proton (b) and X-ray radiation (c & d), imaged with a magnification of 20×

B.3. Python Code for Ki-67 Image Analysis

Listing B.2: Python script for automated Ki-67-positive cell quantification of multiple images

```
1
2  # Ki67 Proliferation Analysis - Multiple Screenshot Images
3
4  from pathlib import Path
5  import cv2
6  import numpy as np
7  import pandas as pd
8  import matplotlib.pyplot as plt
9  from skimage import filters, morphology, segmentation, feature, measure
10 from scipy import ndimage as ndi
11
12 folder = Path(r"path_to_folder")  # Folder with images
13 scale_bar_um = 20            # Scale bar length in µm
14 scale_bar_px = 46            # Scale bar length in pixels (measured in ImageJ)
15 min_area_um2 = 75            # Exclude objects smaller than this (µm²)
16 max_area_um2 = 1500          # Exclude objects larger than this (µm²)
17 watershed_min_distance_um = 5.0  # Expected minimal separation between nuclei centers (µm)
18 intensity_threshold = 75     # Mean pixel intensity threshold for Ki-67 positivity
19
20 # Pixel size and pixel area
21 px_um = scale_bar_um / scale_bar_px
22 pixel_area_um2 = px_um * px_um
23 print(f"Pixel␣size␣=␣{px_um:.4f}␣µm/px␣␣→␣␣Pixel␣area␣=␣{pixel_area_um2:.4f}␣µm²")
24
25 summary_rows = []
26
27 # PROCESS EACH IMAGE
28 for image_path in folder.glob("*.png"):
29     print(f"\nProcessing␣{image_path.name}...")
30     im_bgr = cv2.imread(str(image_path))
31     if im_bgr is None:
32         print("Could␣not␣open,␣skipping.")
33         continue
34
35     green = im_bgr[:, :, 1]   # Ki67 signal (green channel)
36
37     # Segmentation
38     img = green.copy()
39     if img.dtype != np.uint8:
40         img = (255 * (img - img.min()) / (img.max() - img.min())).astype(np.uint8)
41     blur = cv2.GaussianBlur(img, (3, 3), 0)
42     th = filters.threshold_otsu(blur)
43     binary = blur > th
44
45     # Remove small objects and close holes
46     min_area_px = max(1, int(np.round(min_area_um2 / pixel_area_um2)))
47     binary = morphology.remove_small_objects(binary, min_size=min_area_px)
48     binary = morphology.binary_closing(binary, morphology.disk(2))
49
50     # Distance transform + watershed
51     distance = ndi.distance_transform_edt(binary)
52     min_dist_px = max(3, int(round(watershed_min_distance_um / px_um)))
53     local_max = feature.peak_local_max(distance,
54                                        indices=False,
55                                        footprint=np.ones((min_dist_px, min_dist_px)),
56                                        labels=binary)
57     markers = ndi.label(local_max)[0]
58     labels_ws = segmentation.watershed(-distance, markers, mask=binary)
59
60     # Measure nuclei
61     props = measure.regionprops(labels_ws, intensity_image=green)
62     rows = []
63     for i, p in enumerate(props):
64         area_um2 = p.area * pixel_area_um2
65         if area_um2 < min_area_um2 or area_um2 > max_area_um2:
66             continue
67         mean_int = p.mean_intensity
```

```
        is_positive = mean_int >= intensity_threshold
        rows.append({
            "label": i + 1,
            "area_um2": area_um2,
            "mean_intensity": mean_int,
            "Ki67_positive": is_positive,
            "centroid_y": p.centroid[0],
            "centroid_x": p.centroid[1]
        })
    df = pd.DataFrame(rows)

    # Summary per image
    total_cells = len(df)
    positive_cells = df["Ki67_positive"].sum()
    fraction_positive = positive_cells / total_cells if total_cells > 0 else np.nan
    summary_rows.append({
        "image": image_path.name,
        "total_cells": total_cells,
        "Ki67_positive": positive_cells,
        "Ki67_negative": total_cells - positive_cells,
        "fraction_positive": fraction_positive
    })

    print(f"Total: {total_cells}, Ki67+: {positive_cells} ({fraction_positive:.1%})")

    # Save per-nucleus CSV
    out_csv = image_path.with_name(image_path.stem + "_Ki67_percell.csv")
    df.to_csv(out_csv, index=False)

    # Overlay visualization
    plt.figure(figsize=(8, 8))
    plt.imshow(green, cmap="gray")
    bound = segmentation.mark_boundaries(np.stack([green]*3, axis=-1)/255.0,
                                         labels_ws, color=(1, 0, 0))
    plt.imshow(bound, alpha=0.5)
    for _, row in df.iterrows():
        y, x = row["centroid_y"], row["centroid_x"]
        color = "lime" if row["Ki67_positive"] else "red"
        plt.text(x, y, " ", color=color, fontsize=12, ha="center", va="center")

    plt.title(f"{image_path.name}: Ki67+ green, -Ki67 red")
    plt.axis("off")
    out_png = image_path.with_name(image_path.stem + "_Ki67_overlay.png")
    plt.savefig(out_png, dpi=150, bbox_inches="tight")
    plt.close()

# SAVE SUMMARY CSV
df_summary = pd.DataFrame(summary_rows)
summary_csv = folder / "Ki67_summary.csv"
df_summary.to_csv(summary_csv, index=False)

print("\nSaved folder summary to:", summary_csv)
```

B.4. Results from Ki-67 Image Analysis

Fig. B.2 shows example segmentation overlays of Ki-67–stained images generated using the custom Python code. Green and red markers represent Ki-67+ and Ki-67– nuclei, respectively. The overlays demonstrate the code's ability to distinguish proliferating from non-proliferating cells in both chip- and coverslip-cultured samples under different imaging magnifications. As seen in the images, segmentation performance varies depending on cell density and image contrast, which may contribute to small variations in the quantification of Ki-67+ cells.

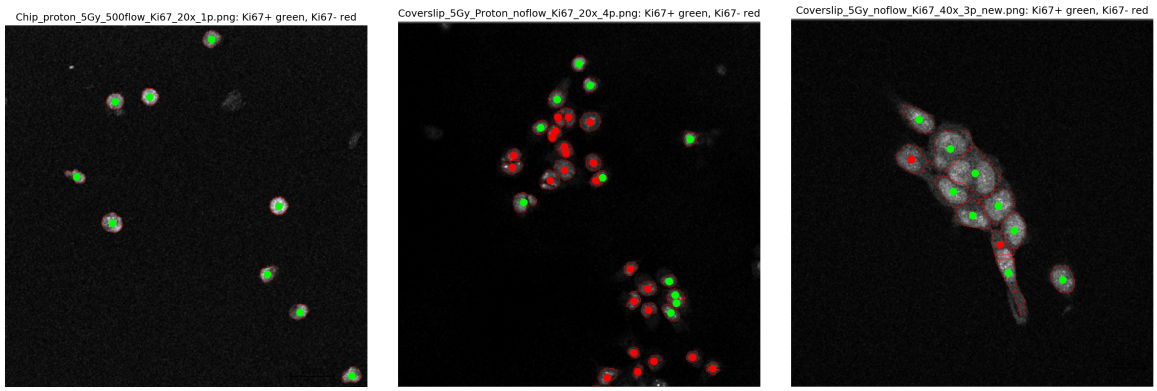

(a) **(b)** **(c)**

Figure B.2: Several Ki-67 segmentation overlay images produced after processing Ki-67-stained images with a custom Python code, where the green and red dots represent Ki-67+ and Ki-67- cells, respectively (a) shows the result of image processing chip-cultured cells exposed to medium flow (500 µL/h) and 5 Gy proton radiation, imaged with a magnification of 20×. (b) and (c) show the results of image processing coverslip-cultured cells, exposed to 5 Gy proton radiation, imaged with a magnification of 20× and 40×, respectively